Energy & Environmental Science

ROYAL SOCIETY OF CHEMISTRY

REVIEW

View Article Online
View Journal | View Issue

Cite this: *Energy Environ. Sci.*, 2021, **14**, 2883

High-entropy energy materials: challenges and new opportunities

Yanjiao Ma, *[a] Yuan Ma, [a] Qingsong Wang, [a] Simon Schweidler, [a] Miriam Botros, [a] Tongtong Fu, [b] Horst Hahn, [ac] Torsten Brezesinski *[a] and Ben Breitung *[a]

The essential demand for functional materials enabling the realization of new energy technologies has triggered tremendous efforts in scientific and industrial research in recent years. Recently, high-entropy materials, with their unique structural characteristics, tailorable chemical composition and correspondingly tunable functional properties, have drawn increasing interest in the fields of environmental science and renewable energy technology. Herein, we provide a comprehensive review of this new class of materials in the energy field. We begin with discussions on the latest reports on the applications of high-entropy materials, including alloys, oxides and other entropy-stabilized compounds and composites, in various energy storage and conversion systems. In addition, we describe effective strategies for rationally designing high-entropy materials from computational techniques and experimental aspects. Based on this overview, we subsequently present the fundamental insights and give a summary of their potential advantages and remaining challenges, which will ideally provide researchers with some general guides and principles for the investigation and development of advanced high-entropy materials.

Received 17th February 2021,
Accepted 1st April 2021

DOI: 10.1039/d1ee00505g

rsc.li/ees

Broader context

The energy crisis and environmental issues caused by the burning of fossil fuels are major challenges facing mankind. In recent years, the pursuit of renewable energy sources and the development of sustainable energy technologies have become important research targets. Various technologies have been used to convert and store energy from clean sources, such as fuel cells, batteries and solar cells, to name a few, and are receiving increasing attention and recognition. One of the keys to their commercialization is to explore functional materials. High-entropy materials, proposed for the first time in 2004, represent a promising class of disordered multicomponent materials with tailorable properties/functionalities (and potentially unprecedented performances) and have been used in a variety of systems and applications. The initial intention was to obtain more robust structures by maximizing the configurational entropy, which resulted in the well-known high-entropy alloys and the later developed high-entropy oxides. Owing to the entropy-driven effects and their chemical and structural diversity, high-entropy materials show much promise in the field of sustainable energy storage and conversion.

1. Introduction

World energy demand has been growing exponentially in the past decades and is estimated to be doubled to 28 TW by the year 2050, which would be equivalent to 20 billion tons of oil per year.[1] This value is alarming due to the essential limitations on rapidly depleting fossil fuels, which currently present approximately 95% of the global energy consumption.[2] More importantly, the increase in greenhouse gas (GHG) emission produced by burning fossil fuels causes severe environmental issues, especially climate changes and the resulting global warming.[3,4] Eliminating that requires the transition to green, reliable and renewable energy sources, for example, wind, hydropower or solar energy, to name a few.[1] However, even if such a transition can be made, most of the renewable power sources are not continuous power supplies, such as solar panels at night, so that more energy storage and efficient energy conversion systems are indispensable in this field and need to be developed in near future. Furthermore, carbon dioxide capture and conversion is also a viable solution to reduce GHG emission and produce carbon-based fuels.[4]

[a] *Institute of Nanotechnology, Karlsruhe Institute of Technology (KIT), Hermann-von-Helmholtz Platz 1, 76344 Eggenstein-Leopoldshafen, Germany. E-mail: yanjiao.ma@kit.edu, torsten.brezesinski@kit.edu, ben.breitung@kit.edu*
[b] *Faculty of Engineering, University of Waterloo, 200 University Avenue West, Waterloo, Ontario, N2L 3G1, Canada*
[c] *Helmholtz Institute Ulm (HIU) for Electrochemical Energy Storage, Helmholtzstraße 11, 89081 Ulm, Germany*

The realization of these advanced applications largely depends on the development of functional materials. Recently, a new class of materials, so-called high-entropy materials (HEMs), is receiving continuously increasing attention. HEMs give rise to attractive features, including the preference for single-phase solid solutions with simple crystal structures, having attributes exceeding their constituent elements, as well as the possibility for tailoring the functional properties.[5–7] A large number of HEMs, including alloys,[5,7–10] oxides,[11–16] oxyfluorides,[17,18] borides,[19] carbides,[20–22] nitrides,[23] sulfides[24] and phosphides,[25] have been reported in a broad range of utilizations, for example, in thermoelectricity applications, thermal and environmental protections, electrochemical energy storage and various catalytic systems. As a very fresh member of energy storage and conversion materials, HEMs exhibit charming qualities. Compared with conventional metal compounds, large entropy may promote the formation of a single-phase structure with severe lattice distortion (strain). Note that lattice distortions are commonly developing in high-entropy alloys (HEAs)[5,8,9,26,27] and are supportive to gas absorption due to the formation of more suitable reaction sites, leading to promising properties, especially for hydrogen storage.[10,28–30] The strong synergistic effects among the functional units are beneficial to the catalysis of energy conversion processes, boosting the investigation of high-entropy noble-metal and noble-metal-free electrocatalysts in methanol oxidation[31–36] as well as oxygen evolution[25,37–47] and reduction.[31,32,45,46,48–52] In the battery field, HEMs also exhibit attractive properties. A unique entropy-stabilized conversion mechanism was proposed for rock-salt high-entropy oxides (HEOs) as lithium storage anodes, leading to improved cycling stability and Coulombic efficiency.[12,17,18,53,54] Also, layered O3-type HEOs were investigated as intercalation-type cathodes

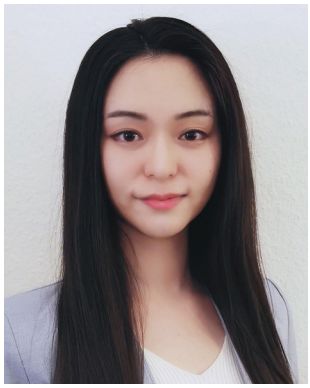

Yanjiao Ma

Yanjiao Ma is currently a post-doctoral researcher at the INT (KIT), where she is developing advanced functional materials, including high-entropy materials for various battery technologies, and mesostructured metal oxide thin films. In 2019, she completed her PhD in Physical Chemistry with Prof. Passerini and Dr. Bresser from the Helmholtz Institute Ulm/KIT, investigating nanostructured materials for alkali-ion batteries. Prior to this, she obtained her Master's degree from the Northwest Normal University in 2015 under the supervision of Prof. Wang, studying nanomaterials and their application as electrocatalysts.

Yuan Ma

Yuan Ma is currently a post-doctoral researcher at the INT (KIT), where he develops coating strategies for cathode materials for all-solid-state battery applications. In 2019, he completed his PhD in Physical Chemistry with Prof. Passerini from the Helmholtz Institute Ulm/KIT, studying metal oxide/sulfide-carbon composites as electrode materials for Li-, Na-, and Zn-ion batteries. Prior to this, he obtained his Master's degree from the Northwest Normal University in 2015, where he investigated the noncovalent interaction for organic supramolecular chemistry.

Torsten Brezesinski

Torsten Brezesinski obtained his PhD from the Max Planck Institute of Colloids and Interfaces/ University of Potsdam with Prof. Antonietti. After postdoctoral work with Prof. Tolbert at the University of California, Los Angeles, he joined the faculty of the Department of Biology and Chemistry at the Justus-Liebig-University Giessen as an independent group leader in 2008. Since 2012, he is laboratory manager of the KIT/BASF SE Battery and Electrochemistry Laboratory (BELLA) and group leader at the INT (KIT). His research focuses on next-generation battery materials for energy storage and polymer-templated mesostructured metal oxide thin films.

Ben Breitung

Ben Breitung is currently working on his habilitation project at the INT (KIT) with Prof. Hahn. In 2013, he obtained his PhD from the KIT, and then joined the Battery and Electrochemistry Laboratory (BELLA) in 2014. Since 2017, he is group leader of the printed electronics group and of the high-entropy materials group at the INT (KIT). His work is focused on high-entropy materials for energy storage and electronic applications and porous thin films.

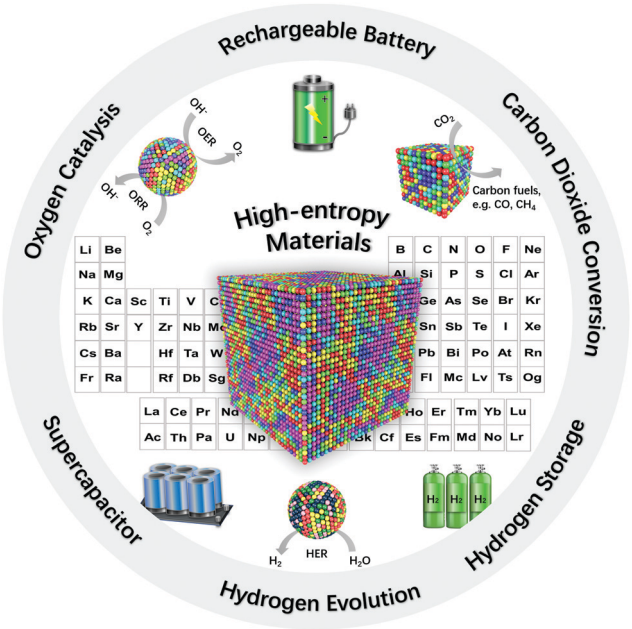

Fig. 1 Schematic of high-entropy materials for applications in energy storage and conversion. Some elements have been omitted for clarity.

towards sodium/lithium storage, showing good long-term cyclability and rate performance owing to entropy stabilization of the host matrix.[13,55]

In this article, we provide a comprehensive overview by focusing on the applications of HEMs, which can be mainly classified in HEAs, high-entropy ceramics (HECs), as well as some other high-entropy composites, in fields of hydrogen evolution and storage, carbon dioxide conversion, oxygen catalysis, rechargeable batteries and supercapacitors (Fig. 1). The (potential) advantages and challenges related to the development of HEMs are systematically discussed. We conclusively extract possible fundamental insights and the most core directions for designing new materials of the high-entropy family, which shall enlighten scientists to develop advanced HEMs for applications in energy storage and conversion.

2. Theoretical concept and structural diversity

The general high-entropy concept was first deployed at the HEAs and can be traced back to two independent studies in 2004.[56,57] Yeh and coworkers first proposed and introduced the concept of HEAs,[56] in the same year, independently, Cantor *et al.*[57] reported a similar study on 5-component single-phase alloys, without mentioning the term ''high-entropy'' but referring to ''multicomponent alloys''. Since then, HEAs have been rapidly developed, often considered as a breakthrough in the field of multicomponent alloy systems. There are two main definitions of HEAs, one is based on composition, while the other is based on configurational entropy.[5,27] In the first definition, HEAs refer to alloys that contain at least five principal elements and each with an atomic percentage in the range of 5% to 35%.[56] If there are any minor elements, then the atomic percentage of each should be less than 5%.[58] For the latter definition, HEAs are defined as alloys with configurational entropies larger than $1.5R$ in a random state, irrespective of whether they are single-phase or multiphase at room temperature.[59] Accordingly, materials with $\Delta S \geq 1.5R$ are categorized as high-entropy class, while materials with $1.0R \leq \Delta S \leq 1.5R$ and $\Delta S < 1.0R$ are classified as middle (or medium)-entropy and low-entropy class, respectively.[27]

Generally, for a random solid solution, the ideal configurational entropy (ΔS_{conf}) per mole can be given as:[60]

$$\Delta S_{conf} = -R\sum_{i=1}^{n} x_i \ln x_i, \quad (1)$$

where R is the ideal gas constant and x_i represents the molar fraction of the ith component. For a given number of components (n), configurational entropy reaches the largest value when the atomic fraction of all components is the same (*i.e.*, equimolar). Then, the configurational entropy per mole is:[27]

$$\Delta S_{conf} = -R\left(\frac{1}{n}\ln\frac{1}{n} + \frac{1}{n}\ln\frac{1}{n} + \cdots + \frac{1}{n}\ln\frac{1}{n}\right) = -R\ln\frac{1}{n} = R\ln n. \quad (2)$$

In the high-entropy concept, ΔS_{conf} solely depends on the number of incorporated elements, thus creating a competitive situation between the additional enthalpy required for mixing different elements (ΔH_{mix}) and the increased ΔS_{mix} based on the Gibbs–Helmholtz equation:[27]

$$\Delta G_{mix} = \Delta H_{mix} - T\Delta S_{mix}. \quad (3)$$

If $T\Delta S_{mix}$ can balance or exceed ΔH_{mix}, entropy stabilization of the crystal structure is established, and the stability of the compound would increase with higher configurational entropy because of the more negative ΔG_{mix}. Additionally, worth to remark that theoretical computations have shown demonstrations, in a multicomponent system a threshold for the number of species is discovered, above such value entropy gain would unavoidably exceed over enthalpy gain and can no longer be ignored.[61]

Various crystal structures of HEAs have been identified, namely, face-centred cubic (fcc), body-centred cubic (bcc), hexagonal close-packed (hcp) and C14 hcp, as presented in Fig. 2a. Many applications of HEAs were reported in the energy sector, including electrochemical energy storage and conversion and hydrogen storage. Yeh *et al.*[58] summarized four core effects of HEAs: (1) high-entropy effects, (2) lattice distortions, (3) sluggish diffusion and (4) cocktail effects. These factors provide HEAs with numerous versatile properties and hence make them suitable for many applications. The presence of lattice distortions in HEAs is due to the different sizes of elements. Because each metal in the HEA has the same probability to occupy the lattice site, severe lattice distortion would arise when ignoring chemical ordering. The mechanical, electrical, thermal, optical and chemical behaviour of materials can be varied by the so-called ''lattice distortion effects''.[10]

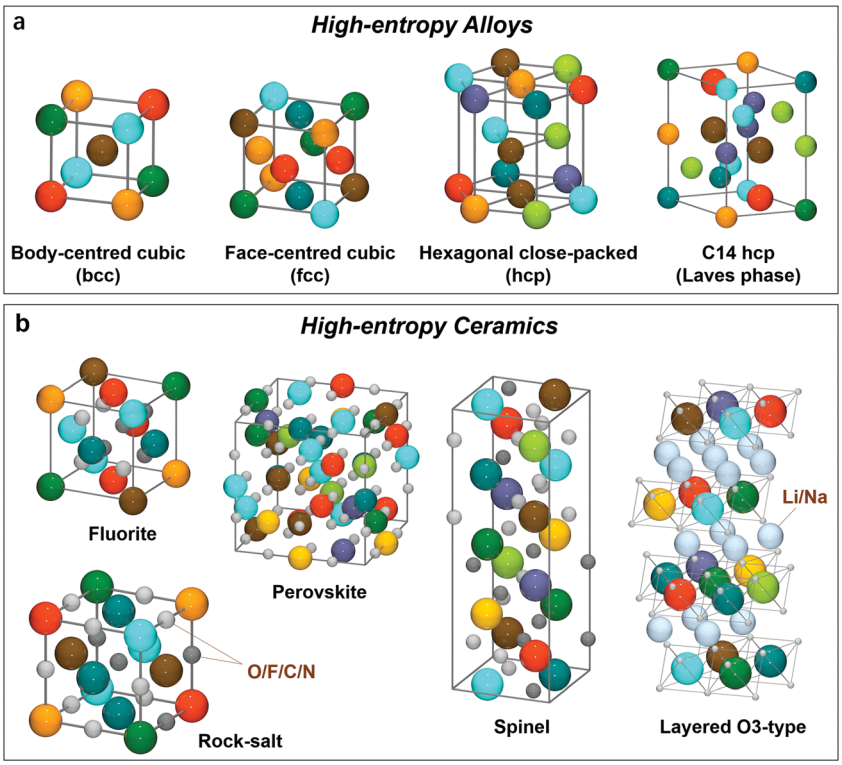

Fig. 2 The identified crystal structures of (a) high-entropy alloys and (b) high-entropy ceramics used in energy-related fields.

For instance, the large lattice strain in the HEAs is beneficial to the absorption of hydrogen in both octahedral and tetrahedral sites, providing great potential for hydrogen energy applications.[10,28–30] Sluggish diffusion effects lead the alloys to develop nanocrystalline or even amorphous structures, which is promising for electrocatalysis, including methanol oxidation[31,35,62,63] or oxygen evolution[39,41,44,46,47] and reduction.[31,52,64] Overall, HEAs can be regarded as atomic-scale composites, since multiprinciple metals are incorporated and the interactions among the different elements are playing an important role,[8,27,59] resulting in a kind of composite (cocktail) effect on properties.

In 2015, the entropy stabilization concept was first transferred to a multicomponent oxide,[11] initiating the development of HECs.[6,65] The molar configurational entropy of ceramic materials can be obtained based on the following equation:[12,66]

$$\Delta S_{\text{conf}} = -R\left[\left(\sum_{i=1}^{n} x_i \ln x_i\right)_{\text{cation-site}} + \left(\sum_{j=1}^{m} x_j \ln x_j\right)_{\text{anion-site}}\right], \quad (4)$$

where x_i and x_j represent the mole fraction of elements in the cation and anion sites, respectively. Both the structure and composition of single-phase HECs are versatile. The most widely studied materials are rock-salt type HECs, including oxides, nitrides and carbides (Fig. 2b). Early research on the rock-salt structure in the energy field focused on $(Co_{0.2}Mg_{0.2}Cu_{0.2}Ni_{0.2}Zn_{0.2})O$, especially its application as a conversion anode material in lithium-ion batteries (LIBs).[12,53,54] By introducing different metal cations and anions, recent studies have shown the possibility of synthesizing Li-containing rock-salt cathode materials.[18,67] The perovskite structure comprises at least two cation sublattices, both of which can be substituted and shared by multiple metals to form a variety of HECs.[43,68–72] Other lattice structures, such as fluorite,[73–75] spinel[16,76,77] and layered oxides[13,55] were also identified and demonstrated their potential in various energy storage and conversion technologies (Fig. 2b). Entropy stabilization and the occurring interactions between the different incorporated elements endow unique properties of HEMs. In this review, we will focus particularly on the effect that entropy stabilization (and the cocktail effect) has on the applications in electrochemical energy storage, for example, in batteries[12,13,17,18,53,55,69,76–79] and supercapacitors.[23,80–82]

3. Hydrogen energy applications

Hydrogen (H_2) is the most abundant substance in terms of resource availability and is being promoted as a promising energy carrier and fuel source with high efficiency and zero emission.[83–85] In virtue of the molecular being small and simple, the energy contained in 1 kg of H_2 is about 120 MJ, exceeding that of most conventional hydrocarbon-based fuels, and the main by-product is only water after the energy being consumed.[86–88] On the strength of these features, H_2 has been identified as a leading candidate for on-board fuel, which consecutively promotes the development of hydrogen storage and hydrogen evolution reaction research. In this section,

we will focus on the utilization of bcc, fcc and C14 hcp structured HEAs in the hydrogen energy field.

3.1 Hydrogen storage

In practice, being used as a fuel, utilization of H_2 encounters drawbacks, such as the low gaseous density and the large energy consumption from the liquefying process. Another important issue is safety concerns due to the ready-to-flame property of H_2. Therefore, storage of hydrogen is a key factor enabling the development of sustainable hydrogen-based energy systems.[88–91] Gaseous, liquid and solid-state storage systems are the three main systems of hydrogen storage techniques available, chosen based on the corresponding size of storage, the application area and the specific conditions.[88,90] Among those techniques, solid-state storage in the form of metal hydrides provides the most compact technology, offering the highest energy density on a volume basis.[92] Recently, HEMs are receiving increasing attention as a new class of potential hydrogen storage materials. Especially HEAs are considered to be the most promising representatives from the high-entropy class.[7,10,93] Comparing with conventional binary or ternary alloys, solid-solution HEAs have unusual properties, originating from the lattice distortion or cocktail effects coming along with the diversity and number of incorporated elements (5 or more principal elements, each having a certain size). The local environment for each atom is different, which may develop lattice distortions (strain) that eventually provide more suitable interstitial sites for the occupation of hydrogen atoms. Table 1 lists the main hydrogen-storage HEAs reported in recent years, which can be classified into two main categories based on their crystal structures, bcc and C14 hcp Laves phases.

The first HEA class designed for hydrogen storage reported by Kao *et al.*[28] was FeMnCoTiVZr. The $FeMnCoTi_xV_yZr_z$ HEA represents a single AB_2 C14 Laves structure, with Zr and Ti being considered to sit on the A sites, while Fe, Mn, Co and V are located at the B sites. It is concluded that the formation of the single C14 Laves phases is promoted by the high-entropy effect. By adding different elements with similar atomic sizes and chemical/physical features, Gibbs free energy is lowered as the term of $T\Delta S_{mix}$ increases due to an increased configurational entropy in the alloy system. Three forms of HEAs, namely, $FeMnCoTi_{0.5–2.5}VZr$, $FeMnCoTiV_{0.4–3.0}Zr$ and $FeMnCoTiVZr_{0.4–3.0}$, present single C14 Laves phases, and the hydrogen absorption/desorption properties can be enhanced by adjusting the V, Zr and Ti proportion without modifying the original crystal structure. The affinity between the alloy elements and hydrogen determines the enthalpy of hydride formation, which is also the deciding factor of the maximum hydrogen storage capacity [$(H/M)_{max}$]. Ti and Zr are shown to be involved in the hydrogen absorption in both $FeMnCoTi_xVZr$ and $FeMnCoTiVZr_z$, with increased $(H/M)_{max}$ for x and z in the ranges of $0.5 \leq x \leq 2.0$ and $0.4 \leq z \leq 2.3$ (Fig. 3a and b). The $(H/M)_{max}$ reached to 1.8 wt% for $FeMnCoTi_2VZr$ at room temperature. The kinetics of hydrogen absorption and the time required for $FeMnCoTi_xV_yZr_z$ to achieve 90% of its absorption capacity ($t_{0.9}$) were measured and determined. The size of the interstitial sites is proved to be the decisive factor in determining the $t_{0.9}$ and the plateau pressure. The introduction of Ti or Zr enlarged interstitial sites of the alloys and led to the expansion of the crystal lattice due to lower compressive atomic stresses. As a result, the $t_{0.9}$ value and plateau pressure of $FeMnCoTi_xVZr$ and $FeMnCoTiVZr_z$ decrease as x and z increase.

Similar studies were conducted on FeMnCrTiVZr HEAs by Chen *et al.*[94] They showed that substituting Cr for Co enhances the hydrogen absorption properties. Therefore, an effective and simplified way of designing the HEA composition has been indicated, which is favoured by the high-entropy effect in the unique complex system, since tailoring (and optimization) of the hydrogen storage properties can be achieved by varying/exchanging certain elements without changing the crystal structure.

Another C14 Laves structure of FeMnCrNiTiZr was studied by Edalati *et al.*,[95] the $(H/M)_{max}$ of 1.7 wt% with fast kinetics at room temperature was discovered, without the material undergoing any activation treatment. They highlighted three criteria to design FeMnCrNiTiZr that can reversibly store hydrogen at room temperature: (i) the total valence-electron concentration (VEC) in HEAs was set to 6.4; (ii) the AB_2 system was selected to

Table 1 Hydrogen absorption/desorption properties of HEAs reported in the literature

HEA	Method	Structure	Temperature (°C)	Pressure (bar)	Maximum hydrogen storage capacity (wt%)	Ref.
FeMnCoTiVZr	Arc melting	C14 Laves	T_{abs}/T_{des}: RT	p_{abs}: 200	1.8	28
FeMnCrTiVZr	Arc melting	C14 Laves	T_{abs}/T_{des}: 5	p_{abs}: 20	2.17	94
FeMnCrNiTiZr	Arc melting	C14 Laves	T_{abs}/T_{des}: RT	p_{abs}: 100	1.7	95
FeCrNiTiVZr	LENS	C14 Laves	T_{abs}/T_{des}: 50	p_{abs}: 100	1.81	96
FeCrNiTiVZr	Arc melting	C14 Laves	T_{abs}/T_{des}: RT	p_{abs}: 50	1.6	97
TiNbVZrHf	Arc melting	bcc	T_{abs}: 300	p_{abs}: 53	2.7	29 and 30
TiNbZrMoV	LENS	Mixed phases	T_{abs}: 50	p_{abs}: 85	2.3	98
TiNbZrMoV	LENS	bcc	T_{abs}: 50	p_{abs}: 85	0.59	98
TiNbZrTa	Arc melting	bcc	T_{abs}/T_{des}: RT	p_{abs}: 7	1.67	99
TiNbVCr	Arc melting	bcc	T_{abs}/T_{des}: RT	p_{abs}/p_{des}: vacuum-25	1.96	100
TiNbVZr	High-energy ball milling	bcc	T_{abs}: 250	p_{abs}: 30	2.5	101
FeCoNiMgTiZr	High-energy ball milling	bcc	T_{abs}: 350	p_{abs}: 20	1.2	102
FeMnNiCrAlW	High-energy ball milling	bcc	T_{abs}: RT	p_{abs}: atm	0.62	103
LaFeNiMnV	LENS	$\sigma + La(NiMn)_5$	T_{abs}/T_{des}: 35	p_{abs}: 50	0.83	104
FeVCoTiCrZr	Arc melting	Mixed phases	T_{abs}/T_{des}: RT	p_{des}: 1.8	1.88	105

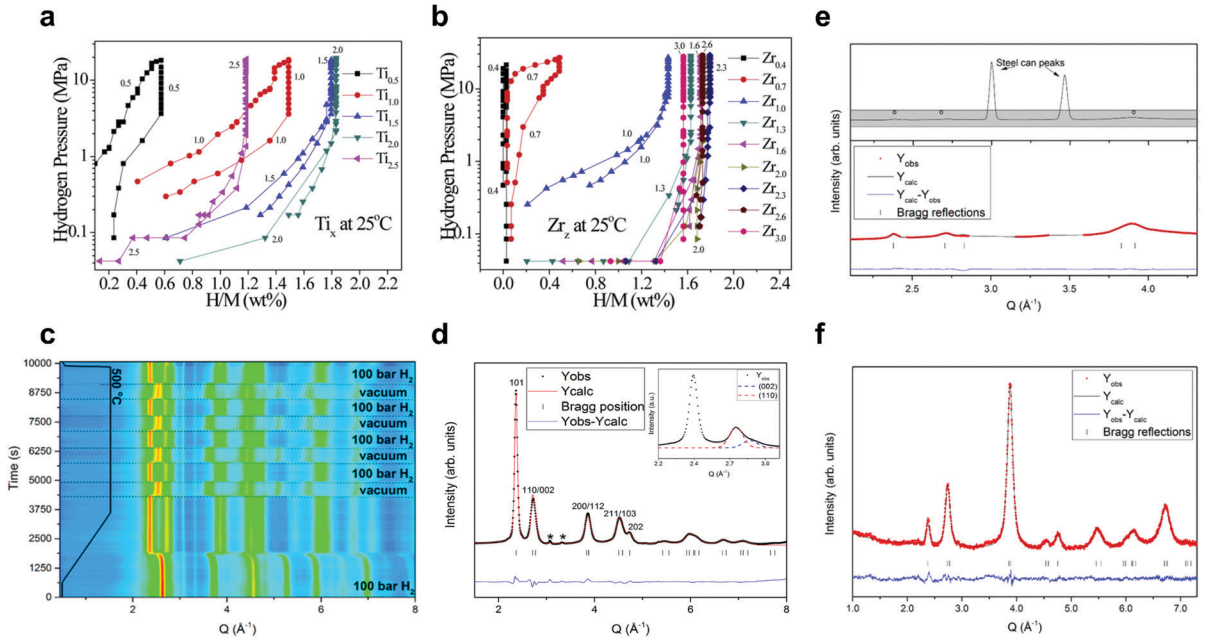

Fig. 3 (a and b) FeMnCoTi$_x$V$_y$Zr$_z$ HEAs: PCIs for (a) various FeMnCoTi$_x$VZr (Ti$_x$) and (b) FeMnCoTiVZr$_z$ (Zr$_z$) materials at 25 °C. Reproduced with permission.[28] Copyright 2010, Elsevier. (c–f) TiNbVZrHf HEA: (c) *in situ* synchrotron-based powder XRD of hydrogen cycling experiments at 500 °C. (d) Rietveld refinement of the hydride structure after 1 cycle absorption–desorption process, with the distorted fcc lattice indicated by the splitting of the 110/002 reflections (inset). (e) *In situ* NPD measurement at 500 °C and 50 bar D_2 and (f) *ex situ* NPD measurement after getting the deuteride. Reproduced with permission.[29] Copyright 2018, American Chemical Society.

reduce the hydrogen binding energy by increasing the number of inert elements around the octahedral sites (A and B refer to the elements that do and do not react with hydrogen, respectively); and (iii) single-phase thermodynamic stability. Kunce *et al.*[96] synthesized a C14 Laves structure-dominated FeCrNiTiVZr *via* the laser engineered net shaping (LENS) process. The $(H/M)_{max}$ reached to 1.81 wt% after synthesis and to 1.56 wt% after additional heat treatment. The same HEA was also produced by Zadorozhnyy *et al.*[97] *via* an arc melting-based rapid solidification process. The greatest hydrogen storage capacity achieved was 1.6 wt% at the first hydrogenation, then it reduced to 1.3–1.4 wt% in the subsequent cycles at ambient temperature. The authors showed results from cyclic voltammetry (CV) and electrochemical impedance spectroscopy (EIS) combined with pressure-composition isotherms (PCI), and calorimetric titrations provided insights into the phase transformations and hydrogen sorption/desorption kinetics (along with the corresponding charge at each potential interval).

Bcc HEAs are widely investigated as hydrogen storage materials, especially alloys composed of refractory elements, since these metals can absorb large amounts of hydrogen, thereby forming hydride phases having a maximum (hydrogen-to-metal) H/M ratio of 2. Sahlberg *et al.*[30] reported a bcc-type TiNbVZrHf, which could be hydrogenated to an H/M ratio of 2.5 in a body-centred tetragonal (bct) structure. It was hypothesized that such high hydrogen storage capacity (greater than any of its constituent elements will absorb) was benefiting from the lattice distortion in the HEA. Similarly, the same composition HEA was also studied by Karlsson *et al.*,[29] a phase transition process (bcc → bct) was carried out, and the results showed the same maximum H/M ratio of 2.5. The hydrogen absorption mechanism was further confirmed by *in situ* X-ray diffraction (XRD) at different temperatures combined with *in situ* and *ex situ* neutron powder diffraction (NPD) measurements. Fig. 3c shows the *in situ* synchrotron-based XRD results from hydrogen cycling experiments at 500 °C, indicating a fully reversible transition from the bcc alloy to a hydride phase (distorted fcc lattice, Fig. 3d). NPD revealed that the hydrogen atoms occupy both the tetrahedral and octahedral interstitial sites in the tetragonal crystal (Fig. 3e and f). The authors concluded that the severe lattice strain in the HEA leads to promising hydrogen storage properties. Interestingly, when studying a similar structured TiNbZrHfTa HEA, Zlotea *et al.*[106] found a two-phase hydrogen absorption reaction, which is in contrast with their previous results for TiNbVZrHf.[30] The hydrogen absorption in TiNbZrHfTa induced a transformation from the initial bcc structure to bct monohydride and eventually to a dihydride phase (fcc). From the comparison between TiNbZrHfTa[106] and TiNbVZrHf,[30] the authors assumed that the phase transformation process is highly related to the lattice distortion (δ), as defined for HEAs:[8] A one-step reaction with hydrogen (bcc → bct hydride with large hydrogen content) would proceed for large δ, while a two-step phase transition (bcc → bct → fcc) is generally promoted by small δ, as also encountered for conventional bcc alloys. However, single-phase bcc TiNbZrMoV[98] has a significantly lower hydrogen storage capacity (0.59 wt%) than that of TiNbVZrHf (2.7 wt%), which is presumably due to

the different hydrogen solubility. In fact, Nb and Mo metals show limited hydrogen solubility, whereas bcc-structured Ti, Hf, V and Zr have rather large hydrogen solubility. Other TiNbZr-based HEAs, such as TiNbZrTa[99] and TiNbZrMoHf,[107] were also investigated, revealing maximum hydrogen storage capacities at room temperature of 1.67 and 1.18 wt%, respectively. The corresponding hydrogen absorption mechanism of TiNbZrTa was shown to be the nucleation and growth mechanism, with rapid hydrogen absorption kinetics, even at room temperature. Furthermore, the authors studied the activation behaviour of TiNbZrTa in another paper,[108] presenting a two-step mechanism comprising the reduction of surface oxides to sub-oxides and the subsequent transformation into sub-hydroxides. TiNbZrMoHf HEAs were also studied on the variation of the concentration of Mo. The results showed a linear relationship between the thermal stability of TiNbZrMoHf hydrides and the Mo content, *i.e.*, the higher the Mo concentration, the lower the stability of TiNbZrMoHf hydrides.

Very recently, Nygård *et al.*[100] reported a series of quaternary and quinary refractory TiNbV-based alloys, including TiNbVX (X = Zr, Cr, Hf, Mo, Ta), TiNbVZrHf, TiNbVCrMo and TiNbVCrTa. This study revealed the importance of VEC in the destabilization of hydrides, suggesting two main interesting trends: (i) from the bcc alloy to the corresponding hydride, the volume expansion of each metal atom increases linearly with the VEC of the alloy (Fig. 4a); and (ii) for hydrogen desorption, the onset temperature decreases linearly with the VEC (Fig. 4b). Based on these insights, TiNbVCr (VEC = 5) was identified to be the most promising hydrogen storage material with 1.96 wt% hydrogen storage capacity at room temperature and without having any activation procedures. Another series of TiNbVTa- and TiNbVZr-based alloys were developed by the same group.[93] All of these materials exhibited single-phase bcc structures, which formed fcc hydrides and reached the maximum H/M ratio of close to 2. Both the bcc and fcc unit cells expand linearly with the Zr/M ratio, and the increase in Zr concentration stabilizes the hydrides. However, the desorption from the Zr-rich hydrides induces phase segregation into two bcc phases, *i.e.*, one with a larger and the other with a smaller unit cell than the original bcc alloy. This is proved by *in situ* synchrotron-based XRD along with the corresponding thermogravimetry/differential scanning calorimetry (TG/DSC) measurements for 4 samples with increasing Zr content (Fig. 4c–f), $TiNbVTaH_x$ (Zr/M = 0), $TiNbVZr_{0.5}Ta_{0.5}H_x$ (Zr/M = 12.5 at%), $TiNbVZrH_x$ (Zr/M = 25 at%) and $TiNbVZr_2H_x$ (Zr/M = 40 at%). This study revealed that excessive Zr in HEAs leads to poor reversibility towards hydrogen absorption/desorption. Following such insight, Montero *et al.*[101] reported a refractory TiNbVZr alloy with a small amount of Zr. The material prepared by the ball-milling method exhibited good stability at the hydrogen storage capacity of around 2 wt%, although a 26% (capacity) fading occurred during the initial cycles.

Some new bcc structures of HEAs, such as FeCoNiMgTiZr,[102] FeMnNiCrAlW[103] and TiZrHfScMo,[109] were also investigated as hydrogen storage materials. Hu *et al.*[109] used density functional theory (DFT) calculations to determine the structural parameters,

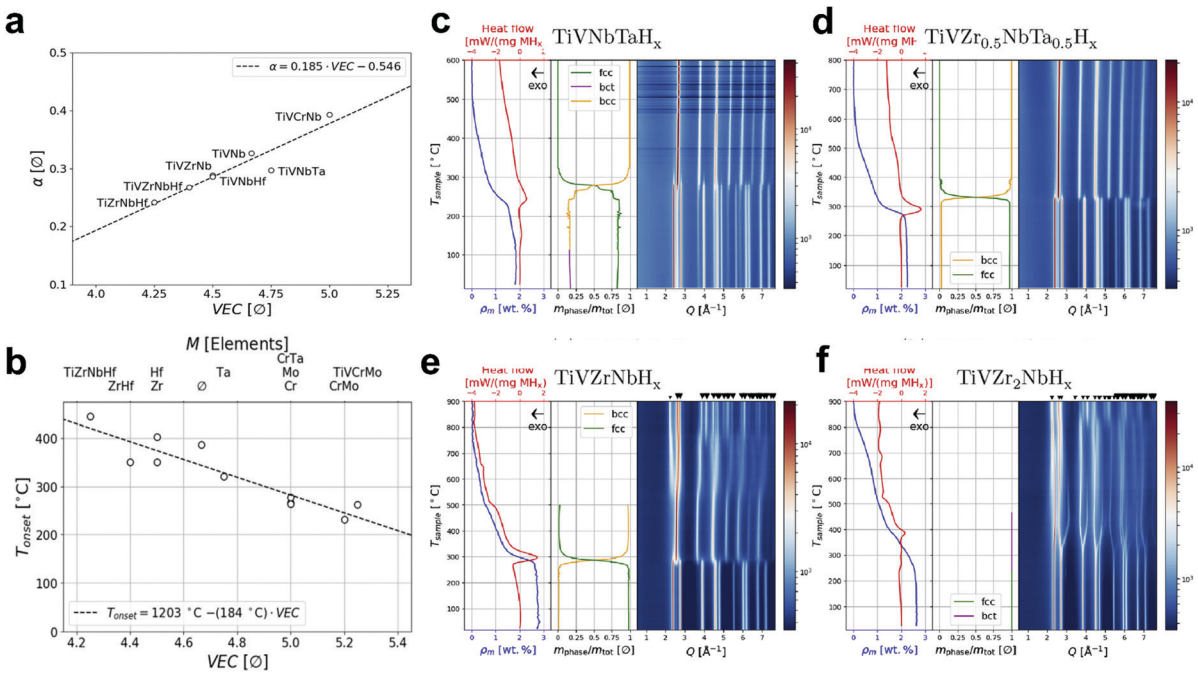

Fig. 4 (a and b) TiNbV-based HEAs: (a) linear correlation between the expansion of the volume of each metal atom and VEC (bcc to the corresponding hydride). (b) Linear correlation between the onset temperature of the second event of hydrogen desorption (bcc monohydride to hydrogen-free bcc alloy) and VEC. Reproduced with permission.[100] Copyright 2019, Elsevier. (c–f) TiNbVTa- and TiNbVZr-based HEAs: *in situ* synchrotron-based XRD measurements during desorption of hydrogen from (c) $TiNbVTaH_x$, (d) $TiNbVZr_{0.5}Ta_{0.5}H_x$, (e) $TiNbVZrH_x$ and (f) $TiNbVZr_2H_x$ and the corresponding TG/DSC analysis and sequential refinement. Reproduced with permission.[93] Copyright 2019, Elsevier.

binding energy and formation enthalpy, as well as the electronic properties of hydrogenated TiZrHfScMo. The first-principles calculations indicated that the hydrogenation is a chemical sorption process, with the possibility of covalent bonding between the metal elements and hydrogen. It was also observed that during the hydrogen absorption process, the different alloy elements are playing different roles, featuring on the advantage of HEMs.

In addition to the C14 Laves and bcc structures, alloys with mixed phases were also reported. For instance, the laser-manufactured LaFeNiMnV showed a primary two-phase structure that changed from initial σ + $La(NiMn)_5$ to fcc + $La(NiMn)_5$ phases, with a maximum hydrogen storage capacity of 0.83 wt%.[104] Multiphase $(FeV)_{60}(CoTiCr)_{40-x}Zr_x$ ($0 \leq x \leq 2$) alloys can quickly absorb hydrogen without any activation process, even at room temperature.[105] For improvements of the hydrogen absorption/desorption kinetics, Ti was substituted by Zr, which can help reduce the microstrain accumulation during the cycles. It is also suggested that a controllable substitution should be considered for optimizing performance, as hydrogen storage capacities decrease with an increased amount of substitution. Nevertheless, it is important to highlight that the properties of HEMs can be fine-tuned by adding species and tailoring concentrations.

3.2 Hydrogen evolution reaction

To date, most hydrogen is being produced by nickel-catalyzed conversion of CH_4 to H_2 and CO or CO_2. However, water electrolysis/splitting has been recognized as an extraordinarily clean and the most promising method for hydrogen production.[110] HEMs are particularly receiving more and more attention for catalytic water splitting. Known procedures include electrocatalytic splitting by PtAuPdRhRu,[111] NiFeMoCoCr,[112] AlNiCuPtPdAu,[32] AlNiCuPtPdAuCoFe[32] and AlNiCuMoCoFe,[32] electrocatalytic splitting by FeCoNiAlTi high-entropy intermetallic (HEI),[113] CoCrFeMnNi-based high-entropy metal phosphide (HEMP)[25] and CoFeLaNiPt high-entropy metallic glass (HEMG),[38] thermochemical splitting by $(FeMgCoNi)O_x$ poly-cation oxide (PCO),[114] as well as photocatalytic splitting by $TiZrHfNbTaO_{11}$ HEO.[68]

Liu *et al.*[111] synthesized carbon-supported PtAuPdRhRu HEA nanoparticles *via* a facile ultrasonication-assisted wet-chemistry method, as shown in Fig. 5a. Benefiting from the strong synergistic effects, the PtAuPdRhRu/C exhibited greater electrocatalytic activity for hydrogen evolution reaction (HER) in an alkaline solution than that of PtAuPdRh/C and commercial Pt/C. A noble-metal-free fcc-type NiFeMoCoCr HEA electrocatalyst was investigated by Zhang *et al.*,[112] providing promising activity in both acidic and alkaline conditions. For instance, in the acidic electrolyte (0.5 M H_2SO_4), the HEA exhibited good HER activity, with a low onset potential (44 mV), small Tafel slope (41 mV dec^{-1}) and low operation overpotential (281 mV) at the current density of 100 mA cm^{-2}.

In addition to the HEAs, some reports also focused on other high-entropy alternatives for electrocatalytic HER. Jia *et al.*[113]

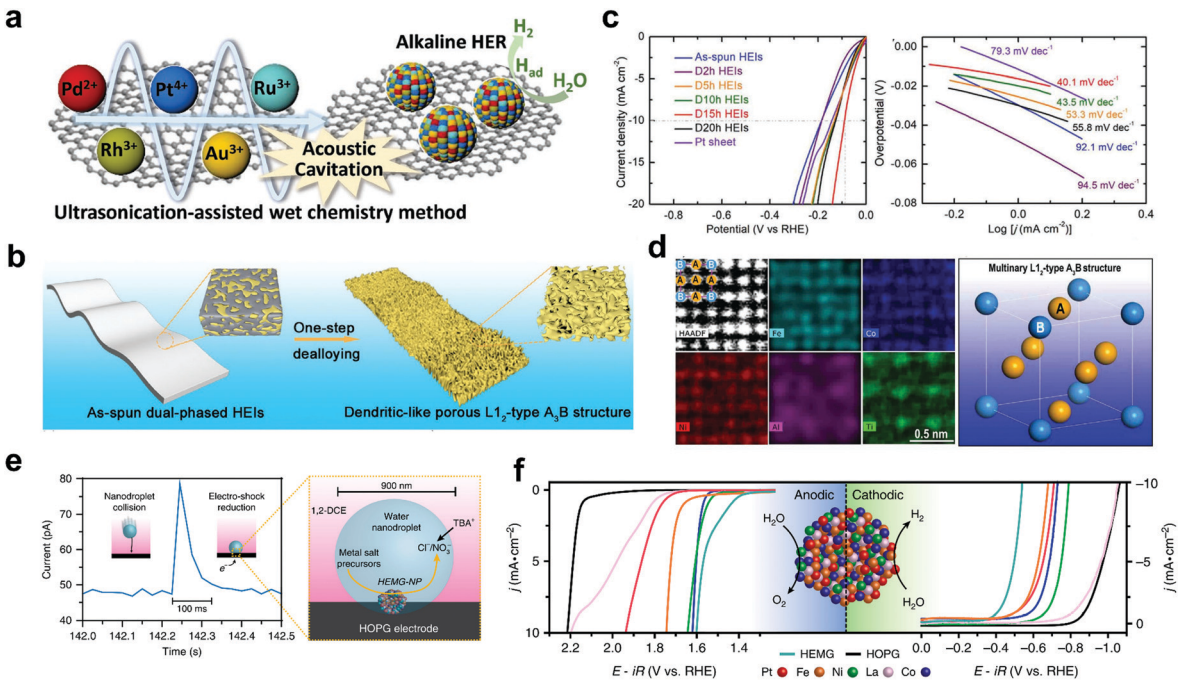

Fig. 5 (a) Schematic diagram of the synthesis of carbon-supported PtAuPdRhRu HEA nanoparticles as HER electrocatalyst. Reproduced with permission.[111] Copyright 2019, Wiley-VCH. (b–d) FeCoNiAlTi HEI: (b) schematic illustration of the dealloying process from a dual-phase structure to a dendritic-like $L1_2$-type structure. (c) Electrocatalytic performance for HER in 1.0 M KOH solution: polarization curves (left) and Tafel slopes at a sweep rate of 5 mV s^{-1} (right). (d) High-magnification high-angle annular dark-field scanning transmission electron microscopy (HAADF STEM) image accompanied by atomic-scale elemental mapping showing the ordered lattice structure (left) and DFT modeling of the site occupancy emphasizing the site-isolated structure (right). Reproduced with permission.[113] Copyright 2020, Wiley-VCH. (e and f) CoFeLaNiPt HEMG nanoparticle electrocatalyst: (e) nanodroplet-mediated electrodeposition for controlling stoichiometry and microstructure. (f) Electrocatalytic evaluation of anodic polarization (left) and cathodic polarization (right) of the HEMG and each of its components. Reproduced under the terms of the CC BY 4.0 license.[38] Copyright 2019, the Authors. Published by Springer Nature.

reported on a non-noble HEI (FeCoNiAlTi) and revealed this surface dendrite-like, well-ordered porous $L1_2$-type structure enables good HER electrocatalytic activity in alkaline condition, with an overpotential of 88.2 mV at the current density of 10 mA cm^{-2} and a Tafel slope of 40.1 mV dec^{-1} (Fig. 5b–d). Glasscott *et al.*[38] reported on a facile one-step nanodroplet-mediated electrodeposition strategy for fabricating HEMG nanoparticles with up to 8 equimolar principle metals, with the capability of controlling precisely the elemental stoichiometry (Fig. 5e). A general synthetic strategy for designing a multifunctional electrocatalyst (CoFeLaNiPt) for both HER and oxygen evolution reaction (OER) was illustrated by combining transition and noble metals with desirable synergistic interactions (Fig. 5f). Zhao *et al.*[25] reported on a single-phase CoCrFeMnNi-based HEMP prepared by an eutectic method and studied the catalytic activity for both HER and OER. Very recently, a high-entropy photocatalyst, $TiZrHfNbTaO_{11}$, was synthesized by Edalati *et al.*,[68] which had dual monoclinic and orthorhombic perovskite phases, and shown to exhibit an appreciable visible light absorption, with a bandgap of 2.9 eV and suitable valence and conduction bands (energy levels) for water splitting.

3.3 Summary of HEMs for hydrogen energy applications

Compared to conventional binary or ternary alloys, the lattice distortions (strain) in HEAs often provide more suitable interstitial sites and diffusion pathways for hydrogen atoms, leading to promising hydrogen storage properties. In addition, HEAs often present highly reversible phase transitions upon hydrogenation/dehydrogenation cycling, which is advantageous to a reversible storage process. Therefore, HEAs represent a good choice to improve the hydrogen storage properties of conventional metal hydrides. On the other hand, when comparing with the rapid developing sorbent materials for hydrogen storage, such as the well-known metal–organic frameworks (MOFs),[115,116] the gravimetric capacity for hydrogen storage in HEAs (typically less than 2.5 wt%) has not yet shown obvious advantages. However, HEAs exhibit superior reaction thermodynamics, which is a known disadvantage of MOF-based materials that require cryogenic temperatures.[116] Also, their properties can be readily tailored through compositional design.

Regarding the application of HEMs for catalytic water splitting, the reported studies are rather limited. However, some high catalytic activities in this field are encouraging. The high-entropy approach can be applied to Pt- or PtRu-based single or binary catalysts and can also be employed in noble-metal-free alloy catalysts to increase their activity by making use of the cocktail effect. In general, it has been observed that HEAs show improved catalytic activity and better stability compared to conventional alloys. Nevertheless, the functionality of individual components is still largely unclear and further experimental research is urgently needed.

4. Oxygen catalysis

Oxygen evolution and reduction reactions (OER and ORR) form the core of various energy conversion technologies, including fuel cells, metal–air (metal–oxygen) batteries and water splitting. The efficiencies of these electrochemical energy conversion systems are severely hampered by sluggish reaction kinetics, requiring the development of electrocatalysts to overcome the energy barriers. HEMs, particularly HEAs of fcc structure, are attracting continuous attention as newly developed catalysts for both OER and ORR.

4.1 Oxygen evolution reaction

HEMs can work as highly efficient electrocatalysts toward the OER both in acid and alkaline conditions. Jin *et al.*[39] synthesized a series of nanoporous Ir-based quinary HEAs, AlCoNiIrX (X = Mo, Cu, Cr, V, Nb), *via* a simple alloying–dealloying strategy, in which the Ir content was only 20 at% (sufficiently less Ir content compared to the common Ir-based binary and ternary alloys with >50 at%). Benefiting from the possible high-entropy and sluggish diffusion effects of HEAs, all of these materials showed good OER activities in an acidic environment. AlCoNiIrMo exhibited the highest OER activity and a substantially enhanced cycling stability (Fig. 6a and b).

Some noble-metal-free HEAs, such as FeNiMnCrCu,[44] FeCoNiCrAl,[44] CoCrFeMnNi,[47] FeCoNiMn[37] and AlCoNiFeX (X = Nb, Mo, Cr),[41,46] were studied in an alkaline environment, showing great potential for future applications as OER electrocatalysts. Qiu *et al.*[41] synthesized several nanoporous AlCoNiFeX (X = Nb, Mo, Cr, V, Zr, Mn, Cu)-based HEAs that have a high-entropy (oxy)hydroxide surface. It was demonstrated that the composition of the alloy plays a crucial role to enhance the OER performance, with AlCoNiFeMo, AlCoNiFeNb and AlCoNiFeCr showing the highest activity (Fig. 6c and d). Furthermore, this group assembled both aqueous and solid-state zinc–air battery cells with AlCoNiFeCr-modified carbon cloth as cathode and a Zn foil anode,[46] showing superior performance compared to Pt/C-IrO_2-based battery cells. Similarly, a core–shell structure of FeCoNiMn-based HEA was investigated by Dai *et al.*[37] Through a CV scan activation, MO_x (M = Fe, Co, Ni, Mn) nanosheets were grown directly onto the FeCoNiMn particle surface, thereby forming the core–shell structure. It was found that such composite exhibits a low overpotential of 302 mV at the current density of 10 mA cm^{-2}, a small Tafel slope of 83.7 mV dec^{-1} and good long-term stability of electrolysis for over 20 h in alkaline conditions, which is comparable to the commercial RuO_2 OER electrocatalyst.

Recently, Wang *et al.*[40] reported a new low-temperature synthesis method for $(CoCuFeMnNi)_3O_4$ HEO nanoparticles with the average particle size of 5 nm. Such HEO nanoparticles showed promising performance toward the OER in an alkaline solution. Some other HEMs, such as high-entropy metal–organic framework (HE-MOF),[42] high-entropy perovskite fluoride (HEPF),[43] HEMG[38] or PCO,[114] were also studied on their OER ability. For instance, Zhao *et al.*[42] reported a MnFeCoNiCu-based HE-MOF synthesized by a facile ambient-temperature solution-phase method (Fig. 6e), demonstrating high electrocatalytic activity for OER in an alkaline system. Wang *et al.*[43] developed a feasible synthesis method for HEPFs by incorporating

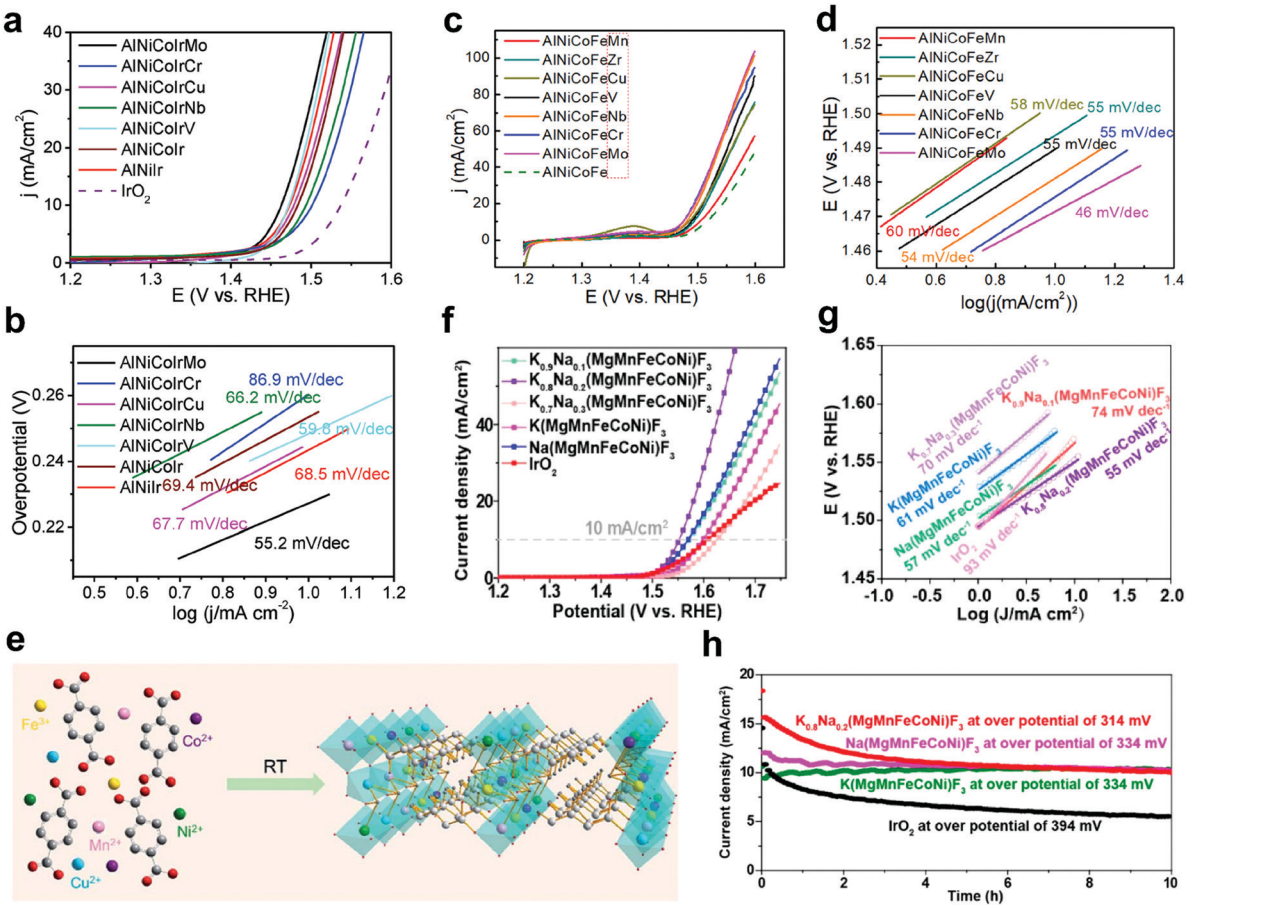

Fig. 6 (a) Linear sweep voltammetry and (b) the corresponding Tafel curves of different AlCoNiIr-based HEAs and IrO_2 in 0.5 M H_2SO_4 solution. Reproduced with permission.[39] Copyright 2019, Wiley-VCH. (c) Linear sweep voltammetry and (d) the corresponding Tafel curves for different AlCoNiFe-based HEAs in 1 M KOH solution. Reproduced with permission.[41] Copyright 2019, American Chemical Society. (e) Synthetic procedure for the preparation of MnFeCoNiCu-based HE-MOF at ambient conditions. Reproduced with permission.[42] Copyright 2019, The Royal Society of Chemistry. (f) Linear sweep voltammetry and (g) the corresponding Tafel curves as well as (h) chronoamperometric recording of IrO_2 and $Na_xK_{1-x}(FeCoNiMnMg)F_3$ in 1 M KOH solution. Reproduced with permission.[43] Copyright 2020, American Chemical Society.

mechanochemistry into hydrothermal reaction, providing a new concept for the preparation of HEMs. These HEPFs (composed of cost-effective elements) showed good catalytic activity for OER in an alkaline solution. For instance, $Na_{0.2}K_{0.8}(FeCoNiMnMg)F_3$ presented superior OER activity with a low overpotential of 314 mV at the current density of 10 mA cm^{-2}, much lower than that of state-of-the-art IrO_2 (Fig. 6f–h).

4.2 Oxygen reduction reaction

Developing new electrocatalysts to improve the kinetics of the sluggish ORR is actively pursued in several energy techniques, such as metal–air batteries and fuel cells. Pt-based nanomaterials are state-of-the-art electrocatalysts in virtue of their excellent catalytic activity toward the ORR. However, most applications are significantly hampered by their scarcity and high costs. Over the past several decades, extensive research efforts have been devoted to developing alternative materials to lower precious-metal loading or exploring noble-metal-free electrocatalysts while maintaining or even enhancing the catalytic activity and durability.

HEMs as newly developed electrocatalysts exhibit promising properties for ORR. Particularly, HEAs with small amounts of Pt, such as PtIrRuCuOs,[31] AlNiCuPtPdAu,[32] AlCuNiPtMn[51] *etc.*, seem to exhibit better activity and stability compared with that of commercial Pt/C catalysts. Nanoporous PtIrRuCuOs with a 3-dimensional bicontinuous ligament/channel structure was synthesized *via* a gentle chemical dealloying of the mechanically alloyed powder precursors. It showed 3.8 times enhancement in the specific activity toward the ORR compared with that of commercial Pt/C, as well as good long-term stability (Fig. 7a and b).[31] Similarly, Qiu *et al.*[32] developed nanoporous AlNiCuPtPdAu with a ligament structure and the composition was precisely controlled by dealloying a customized precursor alloy (Fig. 7c). This HEA exhibited 10 times the mass activity of Pt/C for ORR (Fig. 7d and e), and it showed good activity retention of around 92.5% after 100k cycles. Also, by using the same method, *i.e.*, top-down de-alloying synthesis, the authors reported a series of nanoporous AlNiCuPtX (X = Pd, Ir, Au, V, Co, Mn, Ti, Mo) HEAs and measured the ORR activities in both acidic and alkaline environments.[51] Among them,

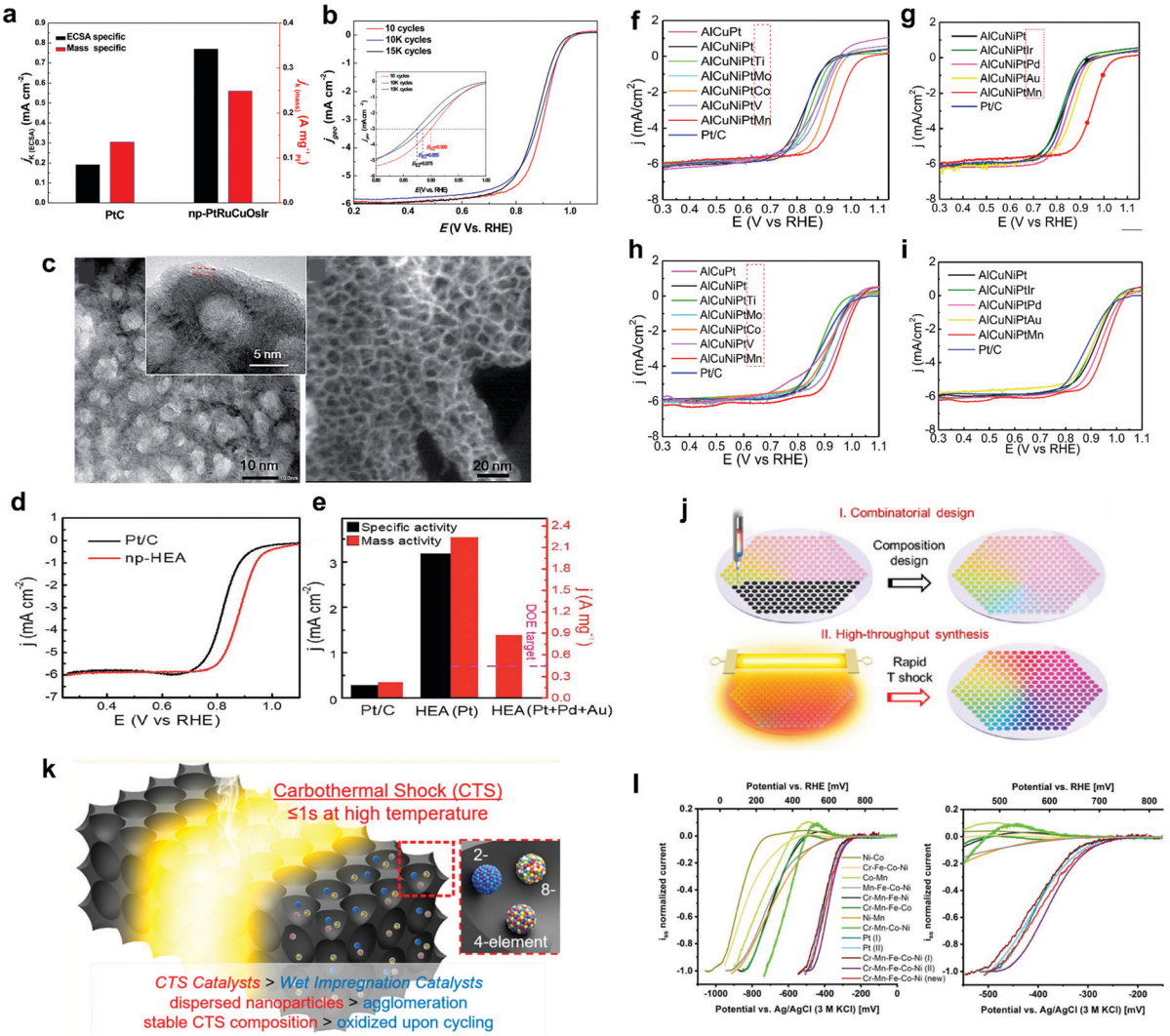

Fig. 7 (a) Electrochemical surface area (ECSA) and mass-specific activities for nanoporous PtIrRuCuOs and Pt/C at 0.9 V *vs.* RHE and (b) ORR polarization curves for the HEA after 10, 10k and 15k cycles in 0.1 M $HClO_4$ solution. Reproduced with permission.[31] Copyright 2015, Elsevier. (c–e) Nanoporous AlNiCuPtPdAu HEA: (c) TEM images at different magnifications, (d) ORR polarization curves and (e) specific and mass activities at 0.9 V *vs.* RHE. Reproduced with permission.[32] Copyright 2019, The Royal Society of Chemistry. (f–i) ORR polarization curves of nanoporous AlNiCuPtX (X = Pd, Ir, Au, V, Co, Mn, Ti, Mo) HEAs and Pt/C in O_2-saturated 0.1 M $HClO_4$ (f and g) and 0.1 M KOH solutions (h and i). Reproduced with permission.[51] Copyright 2020, Elsevier. (j) Schematic illustration of the combinatorial and high-throughput synthesis of uniform multimetallic nanoclusters. Reproduced under the terms of the CC BY-NC-ND 4.0 license.[48] Copyright 2020, the Authors. Published by PNAS. (k) Schematic illustration of the CTS synthesis strategy. Reproduced with permission.[45] Copyright 2019, American Chemical Society. (l) Voltammograms of sputtered nanoparticles (binary, quaternary and quinary CrMnFeCoNi) using an i_{ss} normalized scale for activity comparison. Reproduced with permission.[52] Copyright 2018, Wiley-VCH.

AlNiCuPtMn exhibited the best ORR activity and cycling stability (Fig. 7f–i).

Yao *et al.*[48] reported on the high-throughput synthesis of ultrafine and homogeneous multimetallic nanoclusters, which can be used for developing HEA-based ORR electrocatalysts (Fig. 7j). As a demonstration, the authors prepared a series of ternary (PtPdRh) to octonary (PtPdRhRuIrFeCoNi) nanoclusters and compared the ORR activities in an alkaline solution. A new synthesis method for ORR electrocatalysts, the carbothermal shock (CTS) method, was investigated by Lacey *et al.*,[45] allowing the development of more complex metallic nanoparticle compositions (maximum eight elements) (Fig. 7k). The authors showed that introducing non-catalytically active elements into the individual nanoparticles *via* the CTS approach can result in a further improved stability of electrocatalysts and the battery (lithium–oxygen) lifetime (the higher entropic effect leads to fewer side reactions toward the other cell components). A more theoretical study about HEAs as ORR electrocatalysts was performed through DFT calculations by Batchelor *et al.*[50] The top surface of HEAs provides nearly continuous energy adsorption, resulting from a large number of surface configurations, and the full set of adsorption energies can be spanned out using a simple model. IrPdPtRhRu was studied as an example in this work. By calculating the *OH and *O adsorption energies, the alloy composition with the best predicted catalytic activity was found.

Noble-metal-free-based HEAs, such as CrMnFeCoNi,[49,52] CrMnFeCoNiMo,[49] AlNiCoFeCr[46] *etc.*, were also developed as ORR electrocatalysts. Löffler *et al.*[52] reported about multinary non-noble HEAs generated *via* combinatorial co-sputtering into an ionic liquid. It was found that CrMnFeCoNi exhibits a high activity (similar to that of Pt), which is based on the typical characteristics of its components. Systematic removal of each metal from the quinary alloy led to a significant decrease in activity for all quaternary alloys. This finding indicates that the high-entropy solid solution with a homogeneous distribution of the components leads to a large number of new active sites, resulting in a great potential in terms of tailoring the catalytic properties (Fig. 7l). Furthermore, in a recent study, the authors discussed how adding or substituting elements affects the adsorption energy distribution patterns (AEDPs) and how such influence is reflected in the shape of catalytic curves.[49] This provided a fundamental concept for comprehending the intrinsic catalytic activity of HEAs toward the ORR. Finally, FeCoNiCrMnNb and FeCoNiCrMnMo were proposed as promising candidates (their composition can be further optimized to facilitate the high-scale applications).

4.3 Summary of HEMs for oxygen catalysis

The above studies proved that HEAs are promising candidates for both OER and ORR. The high-entropy approach can be applied to Pt-based noble-metal catalysts by adding more elements to improve their catalytic capabilities by the virtue of synergistic effects and reduce the proportion of noble metal to lower the overall costs. In addition, some noble-metal-free HEA catalysts have also been reported, showing superior performance and particularly increased stability compared to the conventional binary or ternary alloys. The improvements are most probably related to the entropy-driven structure stabilization and the associated effects among the incorporated metals. However, more comparative studies are needed to unveil the role of the individual components. Another general finding is that most of the developed HEA catalysts in this field are 5- or 6-component alloys. Investigations into high-entropy materials with more metal components are required to explore the effect of further increased configurational entropy of the system on catalytic activity.

5. Carbon dioxide conversion

Technologies that can convert carbon dioxide (CO_2) into carbon-based fuels, such as methane (CH_4) or carbon monoxide (CO), are playing a crucial role in sustaining global energy demands and addressing the environmental issues arising from emissions of CO_2.[117] However, the practical applications of the CO_2 reduction reaction (CO_2RR) are currently being challenged due to its low activity and selectivity, as a consequence of the high energy costs coming from the huge kinetic barriers for bonds breaking in CO_2 molecule. Also, the competition of CO_2RR with the HER (standard potentials in the same narrow window, −0.25 V to 0.17 V *vs.* standard hydrogen electrode) in an aqueous environment is another challenge.[118,119] Many efforts have been made to explore high-quality catalysts with specific electronic structures that can promote the CO_2 activation process with high selectivity.[120] Very recently, some groups reported the application of HEMs as electrocatalysts for CO_2 conversion, including the fcc HEAs and rock-salt HEOs.[121–123]

Pedersen *et al.*[121] presented an approach for the investigation of selective and active catalysts toward the CO_2RR and CORR while suppressing the evolution of hydrogen on HEAs. Specifically, CoCuGaNiZn and AgAuCuPdPt were chosen as HEAs, and the related local optimal disordered compositions were predicted (Fig. 8a). The authors demonstrated that the model allows predictions of effective candidate catalysts without having prior knowledge of their catalytic performance. In addition, considering the massive and versatile spaces of HEAs, this approach provides a way to probabilistically optimize the composition in terms of optimal catalytic activity. Interestingly, at the same time, Nellaiappan *et al.*[123] reported a study on the catalytic activity of AgAuCuPdPt HEA toward the CO_2 conversion (Fig. 8b), complementing with the unbiased predictions made by the Pedersen *et al.*[121] AgAuCuPdPt HEA exhibited high Faradaic efficiency for the gaseous products at a low voltage of −0.3 V *vs.* RHE. Chen *et al.*[122] reported a low-temperature mechanochemical synthesis method for (NiMgCoCuZn)O and Pt/Ru-(NiMgCoCuZn)O HEOs (Fig. 8c). The incorporation of maximum 5 wt% noble metal (Pt and Ru in this study) into (NiMgCoCuZn)O, in the form of single atoms or nanoclusters, led to superior stability at high temperature and good catalytic activity for hydrogenating CO_2 in the atmosphere to CO. It is worth to mention that the entropy is playing a crucial role in terms of CO_2RR stability of the material, which also indicates that multicomponent (complex) systems can be further considered as the host matrix for advanced applications.

6. Other catalytic purposes

Apart from the abovementioned energy storage and conversion systems, HEMs have shown to be effective in several other catalytic applications, such as CO oxidation,[32,72,124,125] ammonia oxidation[126] and decomposition,[127] methanol oxidation[31–36] as well as dye degradation.[128] By using the unique high-entropy-derived properties, future studies on the development of HEMs will create new possibilities to overcome the intrinsic limitations imposed by commonly used materials.

7. Rechargeable batteries

7.1 The application of HEOs in the battery field

Rechargeable (secondary) batteries are the choice of power source for a variety of applications, ranging from small-scale devices (*e.g.*, portable electronics) to e-mobility (*e.g.*, electric vehicles). Especially for the latter, however, there is a strong need for improvements on energy and power densities to meet the consumer demands. HEMs, particularly HEOs, were initially

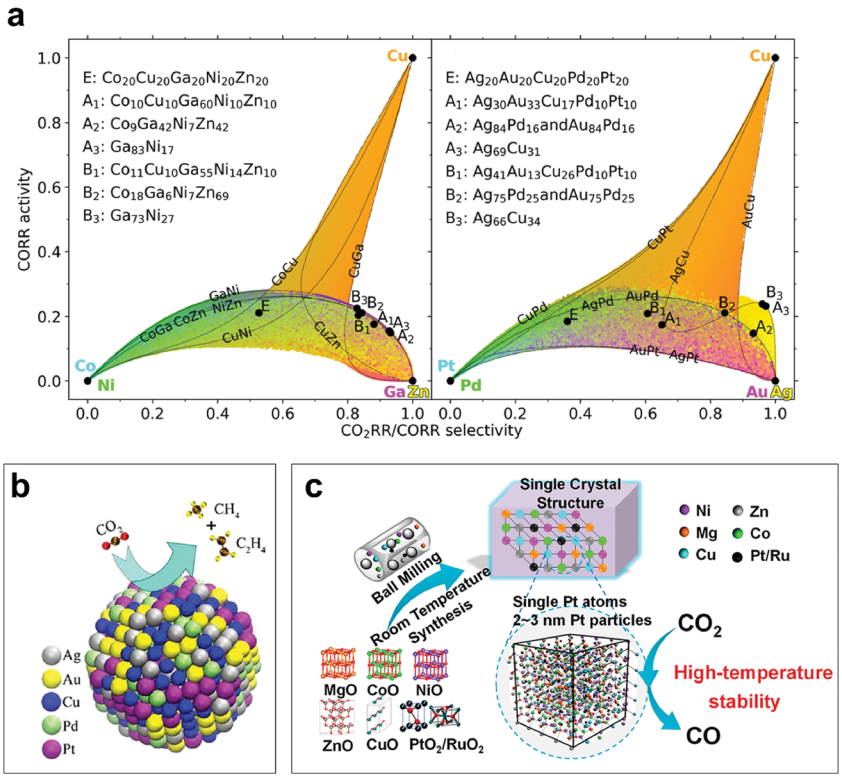

Fig. 8 (a) Plot of the CO_2RR/CORR selectivity and CORR activity space that can be achieved with CoCuGaNiZn (left) and AgAuCuPdPt HEAs (right). Reproduced with permission.[121] Copyright 2020, American Chemical Society. (b) Schematic of the catalytic CO_2 conversion reaction for AgAuCuPdPt HEA. Reproduced with permission.[123] Copyright 2020, American Chemical Society. (c) Schematic of the mechanochemical synthesis of Pt/Ru-(NiMgCoCuZn)O HEO electrocatalyst. Reproduced with permission.[122] Copyright 2019, American Chemical Society.

considered to be employed in batteries due to their superionic conductivity. Bérardan and co-workers prepared single-phase $(CoMgCuNiZn)_{1-x-y}Ga_xA_yO$ (A = Li, Na, K) HEOs with a rock-salt structure. The materials showed high Li-ion conductivity of $>10^{-3}$ S cm^{-1} at room temperature and fast Na mobility (5×10^{-6} S cm^{-1}),[129] making them promising for use as solid electrolytes, for example, in the field of all-solid-state batteries. They demonstrated the conductivity mechanism is based on the ion movement through oxygen deficiencies that are created *via* the charge compensation when monovalent ions are introduced into the pristine HEO. These results were further confirmed by a follow-up study by Osenciat *et al.*,[130] focusing on the compensation mechanism and its relationship with defect structures. The studies have shown for $(CoMgCuNiZn)_{1-x}Li_xO$ solid solutions, up to $x = 0.21$, charge compensation would occur by oxidizing Co^{2+} to Co^{3+}. Beyond the limit of 0.21, the mechanism mainly depends on the oxygen deficiencies. Similarly, further studies explored into the charge-compensating mechanism(s), for example, by DFT calculations[131] or by studying the defect structures.[132] Specifically shown, by optimizing the concentration or sequence of oxygen deficiencies and the size of divalent cations, the ionic conductivity could be improved.

Motivated by these results, HEOs were subsequently studied as electrode materials in rechargeable battery systems (Table 2). Sarkar *et al.*[12] reported on (CoMgCuNiZn)O with a rock-salt structure and its application as anode material in LIBs. The latter cells showed good long-term cycling performance, with a specific capacity of about 650 mA h g^{-1} at 200 mA g^{-1} after 900 cycles and Coulombic efficiencies of >99.5%, despite using micron-sized particles (Fig. 9a). Such high capacity originates from the proposed conversion mechanism, which was proved by the combination of *in situ* XRD and *ex situ* selected-area electron diffraction (SAED) measurements (Fig. 9b and c). Unlike conventional conversion-type materials,[134–139] the rock-salt structure was partially preserved during electrochemical cycling and served as a host for the conversion reaction, which was evidenced by high-resolution TEM (Fig. 9d). In fact, the formed metallic species remained trapped inside the crystal host during the conversion process, facilitating the previously reduced cations to reoccupy the original sites of the HEO lattice.[12] Additionally, using *in situ* differential electrochemical mass spectrometry (DEMS), the authors revealed that a robust solid–electrolyte interphase (SEI) is formed on the surface of HEO particles, even when using an additive-free electrolyte, further emphasizing the advantage of the proposed entropy-stabilized conversion-type lithium storage mechanism.[79] Notably, the HEO system exhibited a great enhancement in terms of cycling stability when compared to medium-entropy oxide materials (Fig. 9e).[12]

(CoMgCuNiZn)O was also used as anode in a full cell study, with $LiNi_{1/3}Co_{1/3}Mn_{1/3}O_2$ (NCM111) serving as the cathode. Such full cells provided an initial specific discharge capacity

Table 2 Charge-storage properties of HEOs reported in the literature

HEOs	Method	Structure	Battery/electrode	Performance	Ref.
(CoMgCuNiZn)O	Nebulized spray pyrolysis	Rock-salt	LIB/anode	770 mA h g^{-1} after 100 cycles at 100 mA g^{-1}	12
(CoMgCuNiZn)O	Nebulized spray pyrolysis	Rock-salt	LIB (full cell)/anode	300 mA h g^{-1} after 50 cycles at 120 mA g^{-1}	17
(CoMgCuNiZn)O	Ball milling, calcination	Rock-salt	LIB/anode	920 mA h g^{-1} after 300 cycles at 100 mA g^{-1}	53
(CoMgCuNiZn)O	Nebulized spray pyrolysis	Rock-salt	LIB/anode	350 mA h g^{-1} after 100 cycles at C/5	79
(CoMgCuNiZn)O	Ball milling, calcination	Rock-salt	LIB/anode	900 mA h g^{-1} after 150 cycles at 200 mA g^{-1}	54
(CoMgNiZnLi)O	Ball milling, calcination	Rock-salt	LIB/anode	720 mA h g^{-1} after 10 cycles at 100 mA g^{-1}	133
Li_x(CoMgCuNiZn)OF_x	Ball milling	Rock-salt	LIB/cathode	120 mA h g^{-1} after 300 cycles at C/10	18
Li_x(CoMgCuNiZn)OF_x	Ball milling	Rock-salt	LIB/cathode	86 mA h g^{-1} after 30 cycles at C/8	79
Li(MnCoCrTiNb)OF	Ball milling, calcination	Rock-salt	LIB/cathode	307 mA h g^{-1} after 20 cycles at 20 mA g^{-1}	67
(CoMgCuNiZn)O	Ball milling, calcination	Rock-salt	Li–S/cathode	768 mA h g^{-1} after 100 cycles at C/10	78
$(TiMgZnFeCu)_3O_4$	Ball milling, calcination	Spinel	LIB/anode	504 mA h g^{-1} after 300 cycles at 100 mA g^{-1}	76
$[(NaBi)_{0.2}(LiLa)_{0.2}(CeK)_{0.2}Ca_{0.2}Sr_{0.2}]TiO_3$	Ball milling, calcination	Perovskite	LIB/anode	85 mA h g^{-1} after 50 cycles at 100 mA g^{-1}	69
$NaCu_{0.12}Ni_{0.12}Mg_{0.12}Co_{0.15}Fe_{0.15}Mn_{0.1}Ti_{0.1}Sn_{0.1}Sb_{0.04}O_2$	Milling, calcination	O3-type	SIB/cathode	80 mA h g^{-1} after 500 cycles at 3C	13

of 446 mA h g^{-1} at 120 mA g^{-1} and still maintained 256 mA h g^{-1} after 100 cycles.[17] Qiu *et al.*[53] reported the improvements in electrochemical performance (*e.g.*, q = 920 mA h g^{-1} at 100 mA g^{-1} after 300 cycles) upon decreasing the particle size to the nanometer level. The authors compared the electrochemical behaviour of (CoMgCuNiZn)O nanoparticles of different sizes prepared by varying the ball milling-duration.[54] The HEO with the smallest particles exhibited the best performance among the materials tested due to increased pseudocapacitive contributions to charge storage (Fig. 9f and g). By substituting Li for Cu, Anik *et al.*[133] reported a rock-salt-type (CoMgNiZnLi)O HEO with a specific capacity of 720 mA h g^{-1} at 100 mA g^{-1} after 10 cycles.

Rock-salt HEMs were also investigated as cathode materials for LIBs. Wang *et al.* synthesized a Li-containing oxyfluoride, $Li_x(Co_{0.2}Mg_{0.2}Cu_{0.2}Ni_{0.2}Zn_{0.2})OF_x$, by milling (CoMgCuNiZn)O and LiF precursors.[18] The introduction of fluorine expanded the working potential to around 3.4 V *vs.* Li^+/Li, compared to 1.0 V for (CoMgCuNiZn)O, thereby providing a great potential to be used as cathode material (Fig. 9h). Benefiting from the high-entropy stabilization, $Li_x(Co_{0.2}Mg_{0.2}Cu_{0.2}Ni_{0.2}Zn_{0.2})OF_x$ showed significant improvements in terms of cycling stability and Coulombic efficiency compared to LiNiOF, which served as a reference electrode material. The redox mechanism was shown to be similar to the insertion/extraction mechanism of disordered Li-rich oxides with a rock-salt structure.[140–144] Although the preliminary results are promising, further optimizations are needed, especially for preventing side reactions due to gas evolution and surface reconstruction and densification, among others.[79,145–148]

Rock-salt (CoMgCuNiZn)O was also investigated as chemical anchor of polysulfides in sulfur cathodes for Li–S cells (Fig. 9i). Specifically, it served to mitigate the shuttle effect caused by the dissolution of lithium polysulfides into the electrolyte.[78] The homogeneously dispersed (multiple) metal species in (CoMgCuNiZn)O strengthened the restriction on lithium polysulfides and facilitated the redox reaction in the cathode (note that the synergistic contribution of Li–O and S–Ni bonds enabled the immobilization of lithium polysulfides in the cathode). As a result, employing (CoMgCuNiZn)O as a kind of catalyst helped to achieve reasonably high specific capacities and low capacity decay for more than 500 cycles (Fig. 9j).

Spinel and perovskite HEOs were also studied as active materials for battery applications. Chen *et al.*[76] reported a spinel-type $(Ti_{0.2}Mg_{0.2}Zn_{0.2}Fe_{0.2}Cu_{0.2})_3O_4$ with fast reaction kinetics and good stability as anode material for LIBs, delivering a specific capacity of 504 mA h g^{-1} at 100 mA g^{-1} after 300 cycles. Wang *et al.*[77] examined the influence of lithium introduction into the lattice structure of a series of spinel materials, $(FeNiMnCoCr)_xO_y$, $(FeNiMnMgCr)_xO_y$ and $(FeNiMnMgZn)_xO_y$. They found when lithium ions were incorporated, a phase transformation occurred from spinel to rock-salt accompanied by partial oxidation of certain elements in the lattice. Yan *et al.*[69] synthesized perovskite $[(NaBi)_{0.2}(LiLa)_{0.2}(CeK)_{0.2}Ca_{0.2}Sr_{0.2}]TiO_3$ *via* a conventional solid-state method and studied the material as anode in LIBs (Fig. 10a and b). The authors attributed the stable performance to the charge-compensation mechanism and the unique entropy-stabilized structure. Commonly, the possibility of accommodating Li^+ in the octahedral interstice is very low, especially when considering the tightly packed perovskite structure. Nevertheless, the existence of high-valence and large-size La^{3+} and Bi^{3+} at the A sites of the perovskite HEO enabled the insertion of additional lithium ions (Fig. 10a). Furthermore, perovskite-type $La_{1-x}Sr_x(FeNiMnCoCr)O_{3-\delta}$ HEOs were synthesized by Dąbrowa *et al.*[70] *via* a sol–gel method, showing potential as air electrode materials for application in solid oxide fuel cells (SOFCs).

Recently, layered HEOs have been shown to exhibit promising lithium storage properties. Zhao *et al.*[13] synthesized a layered O3-type $NaCu_{0.12}Ni_{0.12}Mg_{0.12}Co_{0.15}Fe_{0.15}Mn_{0.1}Ti_{0.1}Sn_{0.1}Sb_{0.04}O_2$ as cathode for sodium-ion batteries (SIBs). The HEO cathode showed good rate capability and long-term cycling stability at different C-rates. For instance, the capacity retention was around 90% after 200 cycles and 83% after 500 cycles at a rate of 3C, with Coulombic efficiencies above 99% during electrochemical cycling (Fig. 10c). Reversible transformation between O3 and P3 phases was observed, with >60% of the total capacity being stored in the region of O3-type (Fig. 10d and e). Compared to the conventional O3 cathode containing three

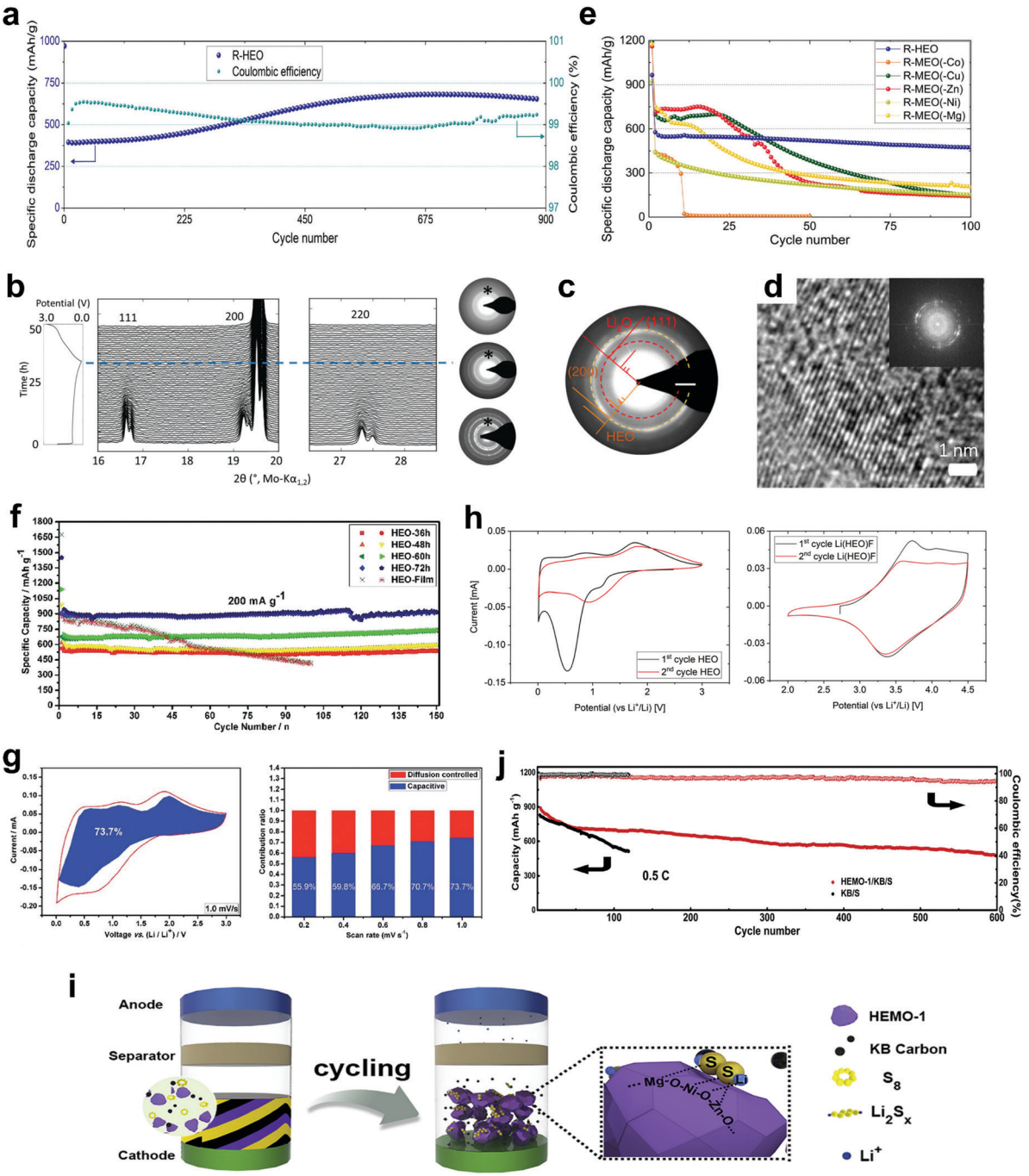

Fig. 9 (a) Cycling performance and Coulombic efficiency of (CoMgCuNiZn)O at 200 mA g^{-1}, (b) *operando* XRD and SAED patterns, (c) SAED pattern for the lithiated HEO and (d) high-resolution TEM image and the corresponding FFT pattern for the cycled sample. (e) Comparison of the cycling performance of high-entropy (CoMgCuNiZn)O (R-HEO) and medium-entropy (4-cation) oxides (R-MEO). Reproduced under the terms of the CC BY 4.0 license.[12] Copyright 2018, the Authors. Published by Springer Nature. Reproduced with permission.[14] Copyright 2019, Wiley-VCH. (f) Comparison of the cycling performance of (CoMgCuNiZn)O with different particle sizes and (g) quantitative capacitive analysis of lithium storage behaviour for the HEO with the smallest particle size. Reproduced under the terms of the CC BY-NC 3.0 license.[54] Copyright 2019, the Authors. Published by The Royal Society of Chemistry. (h) CV curves at 0.1 mV s^{-1} for (CoMgCuNiZn)O in the voltage range of 0.01–3.0 V *vs.* Li^+/Li (left) and Li(CoMgCuNiZn)OF between 2.5 and 4.5 V *vs.* Li^+/Li (right). Reproduced under the terms of the CC BY-NC 3.0 license.[18] Copyright 2019, the Authors. Published by The Royal Society of Chemistry. (i) Schematic diagram of the cell configuration using (CoMgCuNiZn)O HEO as chemical anchor for polysulfides in the cathode of lithium–sulfur cells and (j) long-term cycling performance and Coulombic efficiency of (CoMgCuNiZn)O (HEMO-1/KB/S) and conventional (KB/S) cathodes. Reproduced with permission.[78] Copyright 2019, Elsevier.

transition metal (TM) species, the HEO structure led to more different local interactions between the elements in the TMO_2 slabs and Na in the NaO_2 slabs, as shown in Fig. 10f. During the (de-)sodiation, only some of the TMs participated in the charge

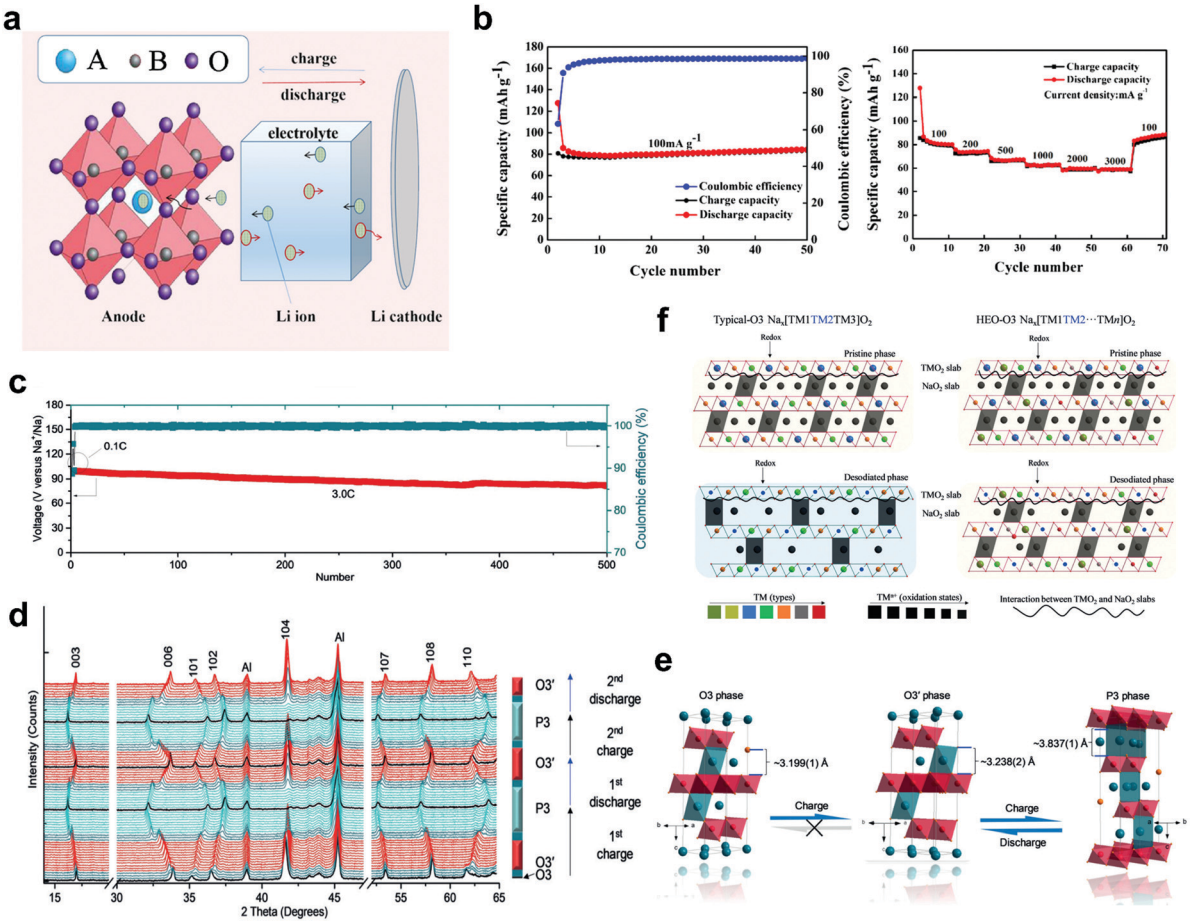

Fig. 10 (a) Schematic representation of the (de-)lithiation process of high-entropy perovskite $[(NaBi)_{0.2}(LiLa)_{0.2}(CeK)_{0.2}Ca_{0.2}Sr_{0.2}]TiO_3$ anode and (b) the corresponding cycling performance at 100 mA g^{-1} and rate capability. Reproduced with permission.[69] Copyright 2020, Springer Nature. (c) Cycling performance and Coulombic efficiency of layered O3-type $NaCu_{0.12}Ni_{0.12}Mg_{0.12}Co_{0.15}Fe_{0.15}Mn_{0.1}Ti_{0.1}Sn_{0.1}Sb_{0.04}O_2$ cathode at 3C rate in SIB cells. (d) *In situ* XRD patterns collected at C/10 rate for the first two cycles, (e) the corresponding crystal structure evolution and (f) schematic diagram of high-entropy composition in promoting the structure of layered O3-type. Reproduced with permission.[13] Copyright 2020, Wiley-VCH.

compensation, this inducing changes of local interactions and leading to further phase transitions. The proposed mechanism suggests that the entropy stabilization assists to facilitate the O3-type structure, resulting in improved cycling stability and rate performance.

Wang *et al.*[55] reported on a series of layered HEO cathodes, $Li(CoNiAlMnZn)_1O_2$, $Li(CoNiAlMnFe)_1O_2$ and $Li_{0.8}Na_{0.2}$-$(CoNiAlMnFe)_1O_2$, with the TM and aluminium cations present in equimolar amounts. Interestingly, upon the incorporation of a small amount of sodium, $Li_{0.8}Na_{0.2}(CoNiAlMnFe)_1O_2$ revealed a much improved electrochemical performance for lithium (de-)intercalation, which is probably due to some widening of diffusion channels of the layer structure. However, the cation disorder might be responsible for the rapid capacity decay.

7.2 Summary of HEMs for battery applications

The above studies have shown that several types of HEOs hold promise as electrode materials for application in rechargeable batteries. The most typical representative is the conversion-type (CoMgCuNiZn)O anode for LIBs. Owing to the proposed entropy-stabilized reaction mechanism, the original lattice structure is partially retained during electrochemical cycling, serving as a host for the conversion process and leading to improved stability. However, although the large entropy and the associated cocktail effects give rise to promising properties, the intrinsic limitations of these conversion-type materials remain:[149] (i) the mean (lithiation) voltage is not very favourable, leading to low overall energy density; (ii) large voltage hysteresis results in poor energy efficiency; and (iii) side reactions, such as continuous electrolyte decomposition, due to extrinsic and intrinsic instabilities strongly affect the cycling performance and stability negatively. Nevertheless, some basic strategies may be used for mitigating such issues: (1) reducing the lithiation voltage (for anodes) by tailoring the composition (*i.e.*, using metals with lower redox potential).[138,150,151] (2) Improving energy efficiency by varying the anion(s). Oumellal *et al.* have shown that the voltage hysteresis strongly depends on the nature of the anion, increasing in the sequence of hydrides < phosphides < nitrides < sulfides < oxides < fluorides.[152] Additionally, switching to phosphides or nitrides,

for example, could potentially result in a better power density because of their higher electronic (ionic) conductivity. (3) Coating HEMs with carbonaceous or polymeric materials to improve the electronic conductivity, buffer the volume variations during cycling and passivate the surface of highly reactive particles in order to stabilize the electrode/electrolyte interface, thereby preventing electrolyte decomposition.[151,153–162] As for the cathode side, no conversion-type HEMs have been reported so far. However, we believe that it is feasible to introduce this conversion mechanism into cathode materials, such as metal fluorides.

Regarding the intercalation-type HEO materials, although there are only two such studies,[13,55] the results reported are very promising. Hence, using layered HEMs may be a good research direction towards next-generation battery technologies. Furthermore, there is a completely vacant field for HEMs in rechargeable batteries, namely, lithium storage by alloying reaction mechanisms,[163] despite the fact that there are many reports on *e.g.*, Zn- or Sn-containing HEAs.

8. Supercapacitors

Supercapacitors are considered as one of the most promising high-power energy storage devices with virtually unlimited cycle life ($>10^6$ cycles).[164] Recently, there have been some reports on HEMs for supercapacitor applications. Kong *et al.*[82] produced a nanoporous metal core/oxide shell structure using equiatomic FeNiCoCrAl HEA through selective phase dissolution and investigated the electrochemical properties. A high volumetric capacitance of 700 F cm^{-3} and superior cycling stability of over 3000 cycles were demonstrated with the binder-free electrode, largely outperforming other nanoporous metals reported so far (Fig. 11a–c).

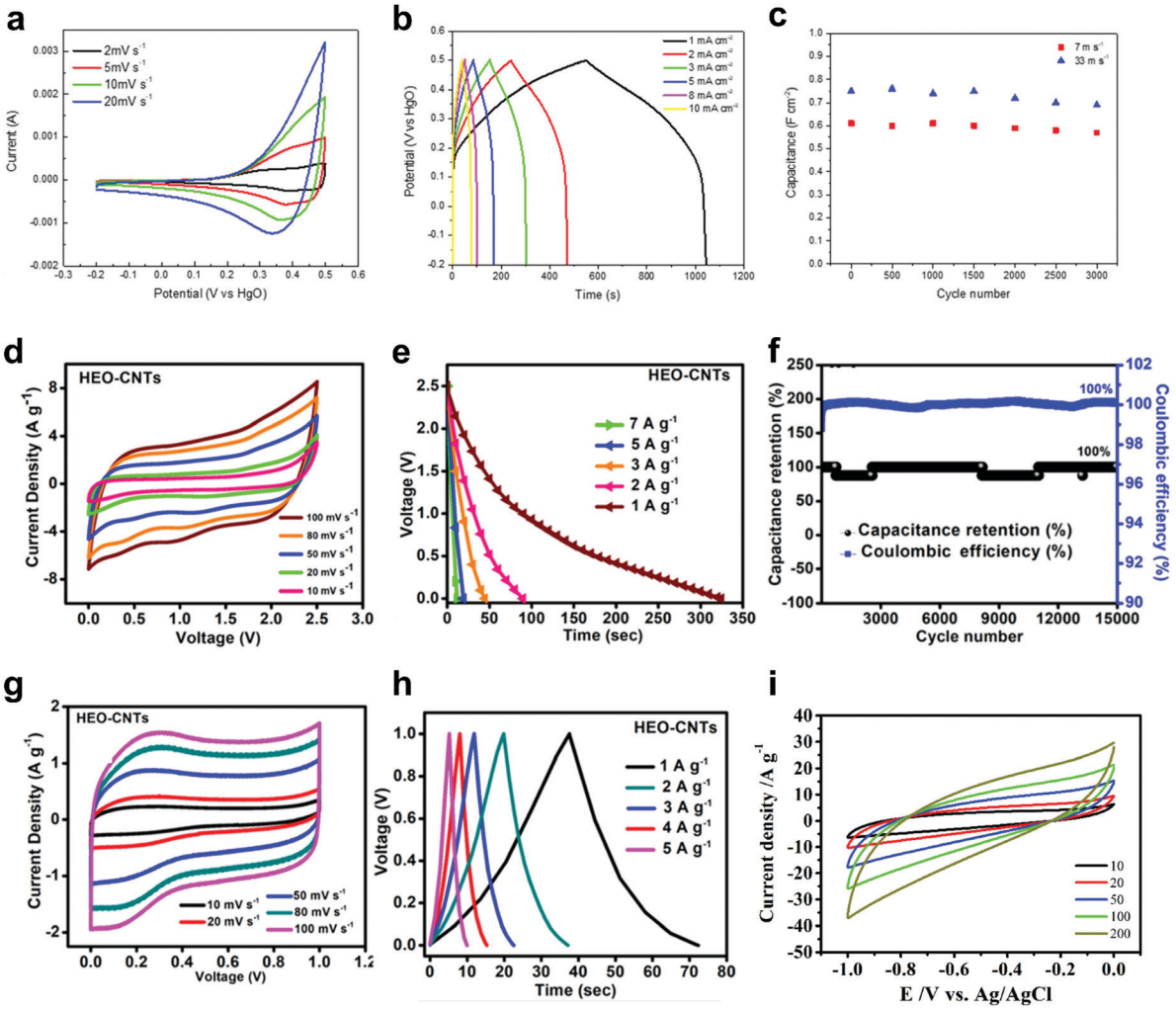

Fig. 11 (a–c) Nanoporous FeNiCoCrAl-based HEA: (a) CV curves at different sweep rates, (b) galvanostatic charge–discharge curves at different current densities and (c) areal capacitance as a function of cycle number at 1 mA cm^{-2}. Reproduced with permission.[82] Copyright 2019, Elsevier. (d–h) FeNiCoCrAl-based HEO–CNT nanocomposite: (d) CV and (e) galvanostatic discharge curves at different sweep rates/specific currents of full cell capacitors using [BMIM][TFSI] electrolyte. (f) Capacitance retention and Coulombic efficiency at 5 A g^{-1}, (g) CV and (h) galvanostatic charge–discharge curves at different sweep rates/specific currents of full cell capacitors using PVA/H_2SO_4 electrolyte. Reproduced with permission.[80] Copyright 2019, American Chemical Society. (i) CV curves for (CrMoNbVZr)N at different sweep rates. Reproduced with permission.[23] Copyright 2018, Wiley-VCH.

Xu *et al.*[81] reported on CTS-derived FeNiCoMnMg HEA nanoparticles on aligned electrospun carbon nanofibers (CNFs). The FeNiCoMnMg/CNF electrodes showed a specific capacitance of 203 F g^{-1} and gravimetric energy density of 21.7 W h kg^{-1}, with a long lifespan of 2000 cycles. Lal *et al.*[80] synthesized FeNiCoCrAl-based HEO nanoparticles employing a sol–gel auto combustion strategy. They used the nanoparticles as catalyst for the chemical vapour deposition (CVD) growth of carbon nanotubes (CNTs). The derived HEO–CNT nanocomposite showed a specific surface area of 151 m^2 g^{-1} and delivered a specific capacitance of 271 F g^{-1} at 1 A g^{-1} when using [BMIM][TFSI] ionic liquid as electrolyte (Fig. 11d and e). In addition, when using PVA/H_2SO_4 as electrolyte, the HEO–CNT nanocomposite exhibited a specific capacitance value of 71 F g^{-1} at 1 A g^{-1}, as well as nearly 100% capacitance retention and Coulombic efficiency up to 15k cycles in a full cell capacitor (Fig. 11f–h).

Jin *et al.* reported a high-entropy metal nitride with 5 highly dispersed metal components, (CrMoNbVZr)N, by using a mechanochemical-assisted soft urea approach.[23] The high-entropy nitride with a cubic crystal structure showed possibilities for supercapacitor applications by delivering specific capacitances ranging from 230 to 54 F g^{-1} for sweep rates of 10 to 200 mV s^{-1} (Fig. 11i) (note that the specific capacitance of 78 F g^{-1} at 100 mV s^{-1} in 1 M KOH solution was about 1.5 times that of reported VN@C nanowire electrodes), presenting new opportunities for utilization of HEMs in energy storage.[165]

9. Computational techniques

In addition to the rapid development of various experimental studies, computational studies on HEMs have also been followed up. Several investigations have been conducted on the DFT and *ab initio* molecular dynamics (AIMD) calculations to guide the materials design, especially for HEAs.[27] However, due to the disordered solid-solution structure and the complexity of the multicomponent high-entropy systems, coupled with the issue of the time-consuming nature of such approaches, those computational techniques are not yet suitable for large-scale screening of HEMs.[166,167] Another strategy has been proposed, CALculation of PHAse Diagrams (CALPHAD) method, which can be used to predict equilibrium phases and as a direct strategy to design HEAs.[27] However, the reliability of the CALPHAD approach depends on the accuracy of the database, and multicomponent systems are remaining vastly unexplored. Recently, more research focused on machine learning (ML),[167–180] which has inherent advantages over traditional modeling and seems more suitable for discovering high-entropy systems. Kaufmann *et al.*[175] proposed a novel high-throughput "ML-HEA" approach for predicting the ability of solid-solution formation. The result is an adaptive learning model, which can be gradually improved by injecting new data as the high-entropy system is explored continuously. ML has also been employed in combination with other techniques. For instance, Kostiuchenko *et al.*[181] developed a combination of ML (based on *ab initio* calculations) with Monte Carlo simulations. This strategy was explored to investigate the phase stability and probe short-range order in HEAs. Wen *et al.*[174] presented a HEA design strategy that combines ML approach with experimental design algorithms to search for HEAs with greater hardness. The designed approach is believed to offer a general recipe for optimization of the multi-component system toward the required properties. Regarding the phase selection in ML for HEAs, Zhou *et al.*[168] made an evaluation of the commonly used rules by developing several ML models and proposed a new one with extra designed parameters. In order to verify this rule, various experiments were performed and the results were highly consistent with the predictions, demonstrating that the proposed technique could be used for designing HEAs. Similarly, a new thermodynamics-based rule was developed by Pei and coworkers.[173] The predictions incorporate fcc, bcc and hcp structures in a high-throughput manner. In the energy field, ML approach can also be applied to optimize compositions and structures of HEMs for electrocatalysts in fuel cells,[182] CO_2 conversion[121] and oxygen catalysis.[50,183]

10. Summary and outlook

Recent research progress has demonstrated that the rather young HEMs hold great potential in energy applications. Major representatives are the well-known HEAs and HEOs. The promising functional properties, such as electrocatalytic activity, gas absorption ability, electrochemical charge storage *etc.*, can be realized by tailoring the components of the high-entropy systems. Compared with conventional materials, some (potential) advantages and the main challenges of HEMs are summarized in the following sections.

10.1 High-entropy alloys *vs.* conventional alloys

Key advantages of HEAs, when comparing with the conventional alloys, are induced by the cocktail effect. Benefiting from the individual incorporated elements, the HEAs system can be regarded as an "atomic composite", often exhibiting unprecedented properties, which also can be readily tailored by changing active/inactive units. Apart from that, the strong synergistic effects among the functional units in HEAs play a decisive role in the activity of both noble and noble-metal-free electrocatalysts in the fields of hydrogen evolution, oxygen evolution and reduction, methanol oxidation and carbon dioxide conversion (see Sections 3–6 above). In addition, in contrast to conventional alloys, severe lattice distortion is generated when forming HEAs, as the incorporated metals may have significantly different atomic sizes. This is beneficial for creating more suitable (reaction) sites, thus leading to promising properties in hydrogen storage applications, among others.

10.2 High-entropy oxides *vs.* conventional oxides

Regarding the energy field, the advantages of HEOs over conventional oxides are less apparent. The majority of HEOs were reported for battery applications by serving as electrode active materials, such as rock-salt (CoMgCuNiZn)O (see Section 7).[12]

While the cycling performance is not yet satisfactory for practical applications, the proposed entropy-stabilized conversion mechanism is promising. Unlike in conventional transition metal oxides, the original rock-salt structure is retained to some degree during electrochemical cycling, serving as a host for the conversion process. The (CoMgCuNiZn)O HEO material clearly outperformed the corresponding medium-entropy oxides, which provides a knowledge link between the entropy-driven structural stability and the improved electrochemical performance. On the other hand, in the intercalation-type layered HEO cathodes, the entropy stabilization can help to facilitate the O3-type structure.

10.3 Challenges and perspectives

Despite all the (potential) inherent advantages of HEMs compared to conventional alloys, oxides and other compounds, there are some apparent challenges regarding their practical usage in the energy sector. First of all, even though the results suggest that the properties of HEMs can be tailored by compositional design, the major challenge is to identify functional units and understand the role of individual elements in certain applications and their relationship with the cocktail effect. In general, the studies conducted so far are still in an early stage, and it appears that the ''tailoring'' is mostly done in a random fashion. Designing HEMs rationally is very challenging at present. One possibility is the above-discussed computational approach by using theoretical methods (see Section 9), especially the newly developed ML techniques, enabling the design of HEMs with desired properties. From an experimental point of view, a more efficient way would be selecting a benchmark model and gradually adding or substituting new elements to change the configurational entropy of the system. For instance, Li_x(CoMgCuNiZn)OF_x[18] and (CoMgNiZnLi)O[133] are variants from the model of the rock-salt (CoMgCuNiZn)O material. Another general strategy is to divide the components into sub-categories according to their roles in the system, and then add or replace the selected element with other similar elements in each category. In the $Li_{1.3}Ti_{0.3}Mn_{0.4}O_{1.7}F_{0.3}$ system, for example, Ti^{4+}–Mn^{3+} combination was used as the baseline model, in which Mn^{3+} is considered as the active redox center and Ti^{4+} is designed as the charge compensator.[67,184] By introducing Mn^{2+}, Co^{2+} and Cr^{3+} (as the supplement of the redox centers) and Nb^{5+} (as the charge compensator), $Li_{1.3}Mn^{2+}_{0.1}Co^{2+}_{0.1}Mn^{3+}_{0.1}Cr^{3+}_{0.1}$-$Ti_{0.1}Nb_{0.2}O_{1.7}F_{0.3}$ was successfully prepared, showing much improved electrochemical performance.[67] Besides the widely developed HEAs and HECs, the exploration of new classes of materials is also highly encouraged. For example, introducing the high-entropy approach into MOFs is a promising design direction, enabling the realization of large entropy at ambient temperature, although there are only two related studies reported so far.[42,185] From a macro perspective, the experience from the materials science community provides us with sketch ideas:[186] fabrication of HEMs with distinct morphology in combination with the utilization of nanotechnology, as well as the construction of HEM-based hybrid materials.

The second challenge is to have a more advanced understanding of the high-entropy concept itself. Comparative studies investigated HEMs and the corresponding medium- or low-entropy materials by extracting one or more elements from the system (see also the theoretical part in Section 2). Such experiments are expected to provide more insights into this issue. Especially comparisons between properties and reaction mechanisms seem indispensable.

Regardless of the above-mentioned challenges, the achievements made so far are encouraging, and there are certainly numerous opportunities for future applications of HEMs in the field of renewable energy.

Conflicts of interest

The authors declare no competing financial interests.

Acknowledgements

H. H., B. B. and T. B. (DigiBat project) acknowledge financial support from the Helmholtz Association. Financial support by the German Research Foundation (to T. B., grant no. BR 3499/5-1, to M. B., grant no. SE 1407/4-2 and to H. H., grant no. HA 1344/43-1) is gratefully acknowledged. Q. W., M. B. and B. B. acknowledge the support from EnABLES and EPISTORE, projects funded by the European Union's Horizon 2020 research and innovation program under grant agreement no. 730957 and 101017709, respectively. T. F. acknowledges the Christian Bürkert Foundation. B. B. acknowledges funding from the Kera-Solar project funded by the Carl Zeiss Foundation.

References

1 D. Larcher and J.-M. Tarascon, *Nat. Chem.*, 2015, **7**, 19–29.
2 J. Chow, R. J. Kopp and P. R. Portney, *Science*, 2003, **302**, 1528–1531.
3 O. Edenhofer, *Climate Change 2014: Mitigation of Climate Change*, 2015, vol. 3.
4 S. Chu, Y. Cui and N. Liu, *Nat. Mater.*, 2017, **16**, 16–22.
5 D. B. Miracle and O. N. Senkov, *Acta Mater.*, 2017, **122**, 448–511.
6 C. Oses, C. Toher and S. Curtarolo, *Nat. Rev. Mater.*, 2020, **5**, 295–309.
7 M. C. Gao, D. B. Miracle, D. Maurice, X. Yan, Y. Zhang and J. A. Hawk, *J. Mater. Res.*, 2018, **33**, 3138–3155.
8 Y. F. Ye, Q. Wang, J. Lu, C. T. Liu and Y. Yang, *Mater. Today*, 2016, **19**, 349–362.
9 R. Kozak, A. Sologubenko and W. Steurer, *Z. Kristallogr. – Cryst. Mater.*, 2015, **230**, 55–68.
10 Y. Zhang, T. T. Zuo, Z. Tang, M. C. Gao, K. A. Dahmen, P. K. Liaw and Z. P. Lu, *Prog. Mater. Sci.*, 2014, **61**, 1–93.
11 C. M. Rost, E. Sachet, T. Borman, A. Moballegh, E. C. Dickey, D. Hou, J. L. Jones, S. Curtarolo and J.-P. Maria, *Nat. Commun.*, 2015, **6**, 8485.
12 A. Sarkar, L. Velasco, D. Wang, Q. Wang, G. Talasila, L. de Biasi, C. Kübel, T. Brezesinski, S. S. Bhattacharya, H. Hahn and B. Breitung, *Nat. Commun.*, 2018, **9**, 3400.

13 C. Zhao, F. Ding, Y. Lu, L. Chen and Y. Hu, *Angew. Chem., Int. Ed.*, 2020, **59**, 264–269.
14 A. Sarkar, Q. Wang, A. Schiele, M. R. Chellali, S. S. Bhattacharya, D. Wang, T. Brezesinski, H. Hahn, L. Velasco and B. Breitung, *Adv. Mater.*, 2019, **31**, 1806236.
15 J. Dąbrowa, M. Stygar, A. Mikuła, A. Knapik, K. Mroczka, W. Tejchman, M. Danielewski and M. Martin, *Mater. Lett.*, 2018, **216**, 32–36.
16 M. Stygar, J. Dąbrowa, M. Moździerz, M. Zajusz, W. Skubida, K. Mroczka, K. Berent, K. Świerczek and M. Danielewski, *J. Eur. Ceram. Soc.*, 2020, **40**, 1644–1650.
17 Q. Wang, A. Sarkar, Z. Li, Y. Lu, L. Velasco, S. S. Bhattacharya, T. Brezesinski, H. Hahn and B. Breitung, *Electrochem. Commun.*, 2019, **100**, 121–125.
18 Q. Wang, A. Sarkar, D. Wang, L. Velasco, R. Azmi, S. S. Bhattacharya, T. Bergfeldt, A. Düvel, P. Heitjans, T. Brezesinski, H. Hahn and B. Breitung, *Energy Environ. Sci.*, 2019, **12**, 2433–2442.
19 J. Gild, Y. Zhang, T. Harrington, S. Jiang, T. Hu, M. C. Quinn, W. M. Mellor, N. Zhou, K. Vecchio and J. Luo, *Sci. Rep.*, 2016, **6**, 37946.
20 E. Castle, T. Csanádi, S. Grasso, J. Dusza and M. Reece, *Sci. Rep.*, 2018, **8**, 8609.
21 X. Yan, L. Constantin, Y. Lu, J. Silvain, M. Nastasi and B. Cui, *J. Am. Ceram. Soc.*, 2018, **101**, 4486–4491.
22 P. Sarker, T. Harrington, C. Toher, C. Oses, M. Samiee, J.-P. Maria, D. W. Brenner, K. S. Vecchio and S. Curtarolo, *Nat. Commun.*, 2018, **9**, 4980.
23 T. Jin, X. Sang, R. R. Unocic, R. T. Kinch, X. Liu, J. Hu, H. Liu and S. Dai, *Adv. Mater.*, 2018, **30**, 1707512.
24 R. Z. Zhang, F. Gucci, H. Zhu, K. Chen and M. J. Reece, *Inorg. Chem.*, 2018, **57**, 13027–13033.
25 X. Zhao, Z. Xue, W. Chen, Y. Wang and T. Mu, *ChemSusChem*, 2020, **13**, 2038–2042.
26 E. P. George, D. Raabe and R. O. Ritchie, *Nat. Rev. Mater.*, 2019, **4**, 515–534.
27 M. C. Gao, J. Yeh, P. K. Liaw and Y. Zhang, *High-Entropy Alloys*, Springer International Publishing, Cham, 2016.
28 Y. F. Kao, S. K. Chen, J. H. Sheu, J. T. Lin, W. E. Lin, J. W. Yeh, S. J. Lin, T. H. Liou and C. W. Wang, *Int. J. Hydrogen Energy*, 2010, **35**, 9046–9059.
29 D. Karlsson, G. Ek, J. Cedervall, C. Zlotea, K. T. Mụller, T. C. Hansen, J. Bednarčík, M. Paskevicius, M. H. Sørby, T. R. Jensen, U. Jansson and M. Sahlberg, *Inorg. Chem.*, 2018, **57**, 2103–2110.
30 M. Sahlberg, D. Karlsson, C. Zlotea and U. Jansson, *Sci. Rep.*, 2016, **6**, 36770.
31 X. Chen, C. Si, Y. Gao, J. Frenzel, J. Sun, G. Eggeler and Z. Zhang, *J. Power Sources*, 2015, **273**, 324–332.
32 H. J. Qiu, G. Fang, Y. Wen, P. Liu, G. Xie, X. Liu and S. Sun, *J. Mater. Chem. A*, 2019, **7**, 6499–6506.
33 A. L. Wang, H. C. Wan, H. Xu, Y. X. Tong and G. R. Li, *Electrochim. Acta*, 2014, **127**, 448–453.
34 C. F. Tsai, P. W. Wu, P. Lin, C. G. Chao and K. Y. Yeh, *Jpn. J. Appl. Phys.*, 2008, **47**, 5755–5761.
35 C. F. Tsai, K. Y. Yeh, P. W. Wu, Y. F. Hsieh and P. Lin, *J. Alloys Compd.*, 2009, **478**, 868–871.
36 K. V. Yusenko, S. Riva, P. A. Carvalho, M. V. Yusenko, S. Arnaboldi, A. S. Sukhikh, M. Hanfland and S. A. Gromilov, *Scr. Mater.*, 2017, **138**, 22–27.
37 W. Dai, T. Lu and Y. Pan, *J. Power Sources*, 2019, **430**, 104–111.
38 M. W. Glasscott, A. D. Pendergast, S. Goines, A. R. Bishop, A. T. Hoang, C. Renault and J. E. Dick, *Nat. Commun.*, 2019, **10**, 2650.
39 Z. Jin, J. Lv, H. Jia, W. Liu, H. Li, Z. Chen, X. Lin, G. Xie, X. Liu, S. Sun and H. Qiu, *Small*, 2019, **15**, 1904180.
40 D. Wang, Z. Liu, S. Du, Y. Zhang, H. Li, Z. Xiao, W. Chen, R. Chen, Y. Wang, Y. Zou and S. Wang, *J. Mater. Chem. A*, 2019, **7**, 24211–24216.
41 H.-J. Qiu, G. Fang, J. Gao, Y. Wen, J. Lv, H. Li, G. Xie, X. Liu and S. Sun, *ACS Mater. Lett.*, 2019, **1**, 526–533.
42 X. Zhao, Z. Xue, W. Chen, X. Bai, R. Shi and T. Mu, *J. Mater. Chem. A*, 2019, **7**, 26238–26242.
43 T. Wang, H. Chen, Z. Yang, J. Liang and S. Dai, *J. Am. Chem. Soc.*, 2020, **142**, 4550–4554.
44 X. Cui, B. Zhang, C. Zeng and S. Guo, *MRS Commun.*, 2018, **8**, 1230–1235.
45 S. D. Lacey, Q. Dong, Z. Huang, J. Luo, H. Xie, Z. Lin, D. J. Kirsch, V. Vattipalli, C. Povinelli, W. Fan, R. Shahbazian-Yassar, D. Wang and L. Hu, *Nano Lett.*, 2019, **19**, 5149–5158.
46 G. Fang, J. Gao, J. Lv, H. Jia, H. Li, W. Liu, G. Xie, Z. Chen, Y. Huang, Q. Yuan, X. Liu, X. Lin, S. Sun and H. J. Qiu, *Appl. Catal., B*, 2020, **268**, 118431.
47 F. Waag, Y. Li, A. R. Ziefuß, E. Bertin, M. Kamp, V. Duppel, G. Marzun, L. Kienle, S. Barcikowski and B. Gökce, *RSC Adv.*, 2019, **9**, 18547–18558.
48 Y. Yao, Z. Huang, T. Li, H. Wang, Y. Liu, H. S. Stein, Y. Mao, J. Gao, M. Jiao, Q. Dong, J. Dai, P. Xie, H. Xie, S. D. Lacey, I. Takeuchi, J. M. Gregoire, R. Jiang, C. Wang, A. D. Taylor, R. Shahbazian-Yassar and L. Hu, *Proc. Natl. Acad. Sci. U. S. A.*, 2020, **117**, 6316–6322.
49 T. Löffler, A. Savan, H. Meyer, M. Meischein, V. Strotkötter, A. Ludwig and W. Schuhmann, *Angew. Chem., Int. Ed.*, 2020, **59**, 5844–5850.
50 T. A. A. Batchelor, J. K. Pedersen, S. H. Winther, I. E. Castelli, K. W. Jacobsen and J. Rossmeisl, *Joule*, 2019, **3**, 834–845.
51 S. Li, X. Tang, H. Jia, H. Li, G. Xie, X. Liu, X. Lin and H. J. Qiu, *J. Catal.*, 2020, **383**, 164–171.
52 T. Löffler, H. Meyer, A. Savan, P. Wilde, A. Garzón Manjón, Y.-T. Chen, E. Ventosa, C. Scheu, A. Ludwig and W. Schuhmann, *Adv. Energy Mater.*, 2018, **8**, 1802269.
53 N. Qiu, H. Chen, Z. Yang, S. Sun, Y. Wang and Y. Cui, *J. Alloys Compd.*, 2019, **777**, 767–774.
54 H. Chen, N. Qiu, B. Wu, Z. Yang, S. Sun and Y. Wang, *RSC Adv.*, 2019, **9**, 28908–28915.
55 J. Wang, Y. Cui, Q. Wang, K. Wang, X. Huang, D. Stenzel, A. Sarkar, R. Azmi, T. Bergfeldt, S. S. Bhattacharya, R. Kruk, H. Hahn, S. Schweidler, T. Brezesinski and B. Breitung, *Sci. Rep.*, 2020, **10**, 18430.

56 J.-W. Yeh, S.-K. Chen, S.-J. Lin, J.-Y. Gan, T.-S. Chin, T.-T. Shun, C.-H. Tsau and S.-Y. Chang, *Adv. Eng. Mater.*, 2004, **6**, 299–303.
57 B. Cantor, I. T. H. Chang, P. Knight and A. J. B. Vincent, *Mater. Sci. Eng., A*, 2004, **375–377**, 213–218.
58 J.-W. Yeh, *JOM*, 2013, **65**, 1759–1771.
59 J.-W. Yeh, *Ann. Chim.*, 2006, **31**, 633–648.
60 B. S. Murty, J.-W. Yeh, R. Srikanth and P. P. Bhattacharjee, *High-Entropy Alloys*, Elsevier, 2019.
61 C. Toher, C. Oses, D. Hicks and S. Curtarolo, *npj Comput. Mater.*, 2019, **5**, 69.
62 Y. Ma, R. Wang, H. Wang, V. Linkov and S. Ji, *Phys. Chem. Chem. Phys.*, 2014, **16**, 3593–3602.
63 Y. Ma, H. Li, H. Wang, X. Mao, V. Linkov, S. Ji, O. U. Gcilitshana and R. Wang, *J. Power Sources*, 2014, **268**, 498–507.
64 Y. Ma, H. Li, H. Wang, S. Ji, V. Linkov and R. Wang, *J. Power Sources*, 2014, **259**, 87–91.
65 R. Z. Zhang and M. J. Reece, *J. Mater. Chem. A*, 2019, **7**, 22148–22162.
66 A. Sarkar, B. Breitung and H. Hahn, *Scr. Mater.*, 2020, **187**, 43–48.
67 Z. Lun, B. Ouyang, D.-H. Kwon, Y. Ha, E. E. Foley, T.-Y. Huang, Z. Cai, H. Kim, M. Balasubramanian, Y. Sun, J. Huang, Y. Tian, H. Kim, B. D. McCloskey, W. Yang, R. J. Clément, H. Ji and G. Ceder, *Nat. Mater.*, 2021, **20**, 214–221.
68 P. Edalati, Q. Wang, H. Razavi-Khosroshahi, M. Fuji, T. Ishihara and K. Edalati, *J. Mater. Chem. A*, 2020, **8**, 3814–3821.
69 J. Yan, D. Wang, X. Zhang, J. Li, Q. Du, X. Liu, J. Zhang and X. Qi, *J. Mater. Sci.*, 2020, **55**, 6942–6951.
70 J. Dąbrowa, A. Olszewska, A. Falkenstein, C. Schwab, M. Szymczak, M. Zajusz, M. Moździerz, A. Mikuła, K. Zielińska, K. Berent, T. Czeppe, M. Martin and K. Świerczek, *J. Mater. Chem. A*, 2020, **8**, 24455–24468.
71 S. Jiang, T. Hu, J. Gild, N. Zhou, J. Nie, M. Qin, T. Harrington, K. Vecchio and J. Luo, *Scr. Mater.*, 2018, **142**, 116–120.
72 F. Okejiri, Z. Zhang, J. Liu, M. Liu, S. Yang and S. Dai, *ChemSusChem*, 2020, **13**, 111–115.
73 J. Gild, M. Samiee, J. L. Braun, T. Harrington, H. Vega, P. E. Hopkins, K. Vecchio and J. Luo, *J. Eur. Ceram. Soc.*, 2018, **38**, 3578–3584.
74 A. J. Wright and J. Luo, *J. Mater. Sci.*, 2020, **55**, 9812–9827.
75 A. Sarkar, C. Loho, L. Velasco, T. Thomas, S. S. Bhattacharya, H. Hahn and R. Djenadic, *Dalton Trans.*, 2017, **46**, 12167–12176.
76 H. Chen, N. Qiu, B. Wu, Z. Yang, S. Sun and Y. Wang, *RSC Adv.*, 2020, **10**, 9736–9744.
77 J. Wang, D. Stenzel, R. Azmi, S. Najib, K. Wang, J. Jeong, A. Sarkar, Q. Wang, P. A. Sukkurji, T. Bergfeldt, M. Botros, J. Maibach, H. Hahn, T. Brezesinski and B. Breitung, *Electrochem*, 2020, **1**, 60–74.
78 Y. Zheng, Y. Yi, M. Fan, H. Liu, X. Li, R. Zhang, M. Li and Z. A. Qiao, *Energy Storage Mater.*, 2019, **23**, 678–683.
79 B. Breitung, Q. Wang, A. Schiele, Đ. Tripković, A. Sarkar, L. Velasco, D. Wang, S. S. Bhattacharya, H. Hahn and T. Brezesinski, *Batteries Supercaps*, 2020, **3**, 361–369.
80 M. S. Lal and R. Sundara, *ACS Appl. Mater. Interfaces*, 2019, **11**, 30846–30857.
81 X. Xu, Y. Du, C. Wang, Y. Guo, J. Zou, K. Zhou, Z. Zeng, Y. Liu and L. Li, *J. Alloys Compd.*, 2020, **822**, 153642.
82 K. Kong, J. Hyun, Y. Kim, W. Kim and D. Kim, *J. Power Sources*, 2019, **437**, 226927.
83 K. T. Møller, T. R. Jensen, E. Akiba and H. Wen-Li, *Prog. Nat. Sci.: Mater. Int.*, 2017, **27**, 34–40.
84 K. Mazloomi and C. Gomes, *Renewable Sustainable Energy Rev.*, 2012, **16**, 3024–3033.
85 J. M. Ogden, *Annu. Rev. Energy Environ.*, 1999, **24**, 227.
86 M. Becherif, H. S. Ramadan, K. Cabaret, F. Picard, N. Simoncini and O. Bethoux, *Energy Procedia*, 2015, **74**, 371–380.
87 J. O. Abe, A. P. I. Popoola, E. Ajenifuja and O. M. Popoola, *Int. J. Hydrogen Energy*, 2019, **44**, 15072–15086.
88 S. Dutta, *J. Ind. Eng. Chem.*, 2014, **20**, 1148–1156.
89 Y. H. Zhang, Z. C. Jia, Z. M. Yuan, T. Yang, Y. Qi and D. L. Zhao, *J. Iron Steel Res. Int.*, 2015, **22**, 757–770.
90 J. O. Abe, A. P. I. Popoola, E. Ajenifuja and O. M. Popoola, *Int. J. Hydrogen Energy*, 2019, **44**, 15072–15086.
91 S. G. Chalk and J. F. Miller, *J. Power Sources*, 2006, **159**, 73–80.
92 M. A. Rosen and S. Koohi-Fayegh, *Energy Ecol. Environ.*, 2016, **1**, 10–29.
93 M. M. Nygård, G. Ek, D. Karlsson, M. Sahlberg, M. H. Sørby and B. C. Hauback, *Int. J. Hydrogen Energy*, 2019, **44**, 29140–29149.
94 S. K. Chen, P. H. Lee, H. Lee and H. T. Su, *Mater. Chem. Phys.*, 2018, **210**, 336–347.
95 P. Edalati, R. Floriano, A. Mohammadi, Y. Li, G. Zepon, H. W. Li and K. Edalati, *Scr. Mater.*, 2020, **178**, 387–390.
96 I. Kunce, M. Polanski and J. Bystrzycki, *Int. J. Hydrogen Energy*, 2013, **38**, 12180–12189.
97 V. Zadorozhnyy, B. Sarac, E. Berdonosova, T. Karazehir, A. Lassnig, C. Gammer, M. Zadorozhnyy, S. Ketov, S. Klyamkin and J. Eckert, *Int. J. Hydrogen Energy*, 2020, **45**, 5347–5355.
98 I. Kunce, M. Polanski and J. Bystrzycki, *Int. J. Hydrogen Energy*, 2014, **39**, 9904–9910.
99 C. Zhang, A. Song, Y. Yuan, Y. Wu, P. Zhang, Z. Lu and X. Song, *Int. J. Hydrogen Energy*, 2020, **45**, 5367–5374.
100 M. M. Nygård, G. Ek, D. Karlsson, M. H. Sørby, M. Sahlberg and B. C. Hauback, *Acta Mater.*, 2019, **175**, 121–129.
101 J. Montero, C. Zlotea, G. Ek, J.-C. Crivello, L. Laversenne and M. Sahlberg, *Molecules*, 2019, **24**, 2799.
102 G. Zepon, D. R. Leiva, R. B. Strozi, A. Bedoch, S. J. A. Figueroa, T. T. Ishikawa and W. J. Botta, *Int. J. Hydrogen Energy*, 2018, **43**, 1702–1708.
103 S. K. Dewangan, V. K. Sharma, P. Sahu and V. Kumar, *Int. J. Hydrogen Energy*, 2020, **45**, 16984–16991.
104 I. Kunce, M. Polański and T. Czujko, *Int. J. Hydrogen Energy*, 2017, **42**, 27154–27164.

105 S. Yang, F. Yang, C. Wu, Y. Chen, Y. Mao and L. Luo, *J. Alloys Compd.*, 2016, **663**, 460–465.
106 C. Zlotea, M. A. Sow, G. Ek, J. P. Couzinié, L. Perrière, I. Guillot, J. Bourgon, K. T. Møller, T. R. Jensen, E. Akiba and M. Sahlberg, *J. Alloys Compd.*, 2019, **775**, 667–674.
107 H. Shen, J. Zhang, J. Hu, J. Zhang, Y. Mao, H. Xiao, X. Zhou and X. Zu, *Nanomaterials*, 2019, **9**, 248.
108 C. Zhang, Y. Wu, L. You, X. Cao, Z. Lu and X. Song, *J. Alloys Compd.*, 2019, **781**, 613–620.
109 J. Hu, H. Shen, M. Jiang, H. Gong, H. Xiao, Z. Liu, G. Sun and X. Zu, *Nanomaterials*, 2019, **9**, 461.
110 J. Greeley, T. F. Jaramillo, J. Bonde, I. Chorkendorff and J. K. Nørskov, *Nat. Mater.*, 2006, **5**, 909–913.
111 M. Liu, Z. Zhang, F. Okejiri, S. Yang, S. Zhou and S. Dai, *Adv. Mater. Interfaces*, 2019, **6**, 1900015.
112 G. Zhang, K. Ming, J. Kang, Q. Huang, Z. Zhang, X. Zheng and X. Bi, *Electrochim. Acta*, 2018, **279**, 19–23.
113 Z. Jia, T. Yang, L. Sun, Y. Zhao, W. Li, J. Luan, F. Lyu, L. C. Zhang, J. J. Kruzic, J. J. Kai, J. C. Huang, J. Lu and C. T. Liu, *Adv. Mater.*, 2020, **32**, 2000385.
114 S. Zhai, J. Rojas, N. Ahlborg, K. Lim, M. F. Toney, H. Jin, W. C. Chueh and A. Majumdar, *Energy Environ. Sci.*, 2018, **11**, 2172–2178.
115 N. L. Rosi, J. Eckert, M. Eddaoudi, D. T. Vodak, J. Kim, M. O'Keeffe and O. M. Yaghi, *Science*, 2003, **300**, 1127–1129.
116 J. Yang, A. Sudik, C. Wolverton and D. J. Siegel, *Chem. Soc. Rev.*, 2010, **39**, 656–675.
117 A. Liu, M. Gao, X. Ren, F. Meng, Y. Yang, L. Gao, Q. Yang and T. Ma, *J. Mater. Chem. A*, 2020, **8**, 3541–3562.
118 J. Qiao, Y. Liu, F. Hong and J. Zhang, *Chem. Soc. Rev.*, 2014, **43**, 631–675.
119 S. Nitopi, E. Bertheussen, S. B. Scott, X. Liu, A. K. Engstfeld, S. Horch, B. Seger, I. E. L. Stephens, K. Chan, C. Hahn, J. K. Nørskov, T. F. Jaramillo and I. Chorkendorff, *Chem. Rev.*, 2019, **119**, 7610–7672.
120 S. Garg, M. Li, A. Z. Weber, L. Ge, L. Li, V. Rudolph, G. Wang and T. E. Rufford, *J. Mater. Chem. A*, 2020, **8**, 1511–1544.
121 J. K. Pedersen, T. A. A. Batchelor, A. Bagger and J. Rossmeisl, *ACS Catal.*, 2020, **10**, 2169–2176.
122 H. Chen, W. Lin, Z. Zhang, K. Jie, D. R. Mullins, X. Sang, S. Z. Yang, C. J. Jafta, C. A. Bridges, X. Hu, R. R. Unocic, J. Fu, P. Zhang and S. Dai, *ACS Mater. Lett.*, 2019, **1**, 83–88.
123 S. Nellaiappan, N. K. Katiyar, R. Kumar, A. Parui, K. D. Malviya, K. G. Pradeep, A. K. Singh, S. Sharma, C. S. Tiwary and K. Biswas, *ACS Catal.*, 2020, **10**, 3658–3663.
124 Z. Zhang, S. Yang, X. Hu, H. Xu, H. Peng, M. Liu, B. P. Thapaliya, K. Jie, J. Zhao, J. Liu, H. Chen, Y. Leng, X. Lu, J. Fu, P. Zhang and S. Dai, *Chem. Mater.*, 2019, **31**, 5529–5536.
125 H. Chen, J. Fu, P. Zhang, H. Peng, C. W. Abney, K. Jie, X. Liu, M. Chi and S. Dai, *J. Mater. Chem. A*, 2018, **6**, 11129–11133.
126 Y. Yao, Z. Huang, P. Xie, S. D. Lacey, R. J. Jacob, H. Xie, F. Chen, A. Nie, T. Pu, M. Rehwoldt, D. Yu, M. R. Zachariah, C. Wang, R. Shahbazian-Yassar, J. Li and L. Hu, *Science*, 2018, **359**, 1489–1494.
127 P. Xie, Y. Yao, Z. Huang, Z. Liu, J. Zhang, T. Li, G. Wang, R. Shahbazian-Yassar, L. Hu and C. Wang, *Nat. Commun.*, 2019, **10**, 4011.
128 Z. Y. Lv, X. J. Liu, B. Jia, H. Wang, Y. Wu and Z. P. Lu, *Sci. Rep.*, 2016, **6**, 34213.
129 D. Bérardan, S. Franger, A. K. Meena and N. Dragoe, *J. Mater. Chem. A*, 2016, **4**, 9536–9541.
130 N. Osenciat, D. Bérardan, D. Dragoe, B. Léridon, S. Holé, A. K. Meena, S. Franger and N. Dragoe, *J. Am. Ceram. Soc.*, 2019, **102**, 6156–6162.
131 Z. Rak, C. M. Rost, M. Lim, P. Sarker, C. Toher, S. Curtarolo, J. P. Maria and D. W. Brenner, *J. Appl. Phys.*, 2016, **120**, 095105.
132 Z. Grzesik, G. Smoła, M. Stygar, J. Dąbrowa, M. Zajusz, K. Mroczka and M. Danielewski, *J. Eur. Ceram. Soc.*, 2019, **39**, 4292–4298.
133 M. Anik and E. Lokcu, *The Eurasia Proceedings of Science, Technology, Engineering & Mathematics (EPSTEM)*, 2019, vol. 7, pp. 329–332.
134 P. Poizot, S. Laruelle, S. Grugeon, L. Dupont and J. M. Tarascon, *Nature*, 2000, **407**, 496–499.
135 J. Cabana, L. Monconduit, D. Larcher and M. R. Palacín, *Adv. Mater.*, 2010, **22**, E170–E192.
136 S. H. Yu, S. H. Lee, D. J. Lee, Y. E. Sung and T. Hyeon, *Small*, 2016, **12**, 2146–2172.
137 C. Wu, S.-X. Dou and Y. Yu, *Small*, 2018, **14**, 1703671.
138 Y. Ma, Y. Ma, G. Giuli, T. Diemant, R. J. Behm, D. Geiger, U. Kaiser, U. Ulissi, S. Passerini and D. Bresser, *Sustainable Energy Fuels*, 2018, **2**, 2601–2608.
139 Y. Ma, Y. Ma, D. Bresser, Y. Ji, D. Geiger, U. Kaiser, C. Streb, A. Varzi and S. Passerini, *ACS Nano*, 2018, **12**, 7220–7231.
140 S. Hy, H. Liu, M. Zhang, D. Qian, B. J. Hwang and Y. S. Meng, *Energy Environ. Sci.*, 2016, **9**, 1931–1954.
141 J. Lee, A. Urban, X. Li, D. Su, G. Hautier and G. Ceder, *Science*, 2014, **343**, 519–522.
142 N. Yabuuchi, M. Nakayama, M. Takeuchi, S. Komaba, Y. Hashimoto, T. Mukai, H. Shiiba, K. Sato, Y. Kobayashi, A. Nakao, M. Yonemura, K. Yamanaka, K. Mitsuhara and T. Ohta, *Nat. Commun.*, 2016, **7**, 13814.
143 R. Chen, S. Ren, M. Knapp, D. Wang, R. Witter, M. Fichtner and H. Hahn, *Adv. Energy Mater.*, 2015, **5**, 1401814.
144 R. A. House, L. Jin, U. Maitra, K. Tsuruta, J. W. Somerville, D. P. Förstermann, F. Massel, L. Duda, M. R. Roberts and P. G. Bruce, *Energy Environ. Sci.*, 2018, **11**, 926–932.
145 D.-H. Kwon, J. Lee, N. Artrith, H. Kim, L. Wu, Z. Lun, Y. Tian, Y. Zhu and G. Ceder, *Cell Rep. Phys. Sci.*, 2020, 100187.
146 A. Boulineau, L. Simonin, J. F. Colin, C. Bourbon and S. Patoux, *Nano Lett.*, 2013, **13**, 3857–3863.
147 J. Lee, J. K. Papp, R. J. Clément, S. Sallis, D.-H. Kwon, T. Shi, W. Yang, B. D. McCloskey and G. Ceder, *Nat. Commun.*, 2017, **8**, 981.
148 M. A. Cambaz, B. P. Vinayan, H. Geßwein, A. Schiele, A. Sarapulova, T. Diemant, A. Mazilkin, T. Brezesinski,

R. J. Behm, H. Ehrenberg and M. Fichtner, *Chem. Mater.*, 2019, **31**, 4330–4340.
149 D. Bresser, S. Passerini and B. Scrosati, *Energy Environ. Sci.*, 2016, **9**, 3348–3367.
150 Y. Ma, Y. Ma, G. Kim, T. Diemant, R. J. Behm, D. Geiger, U. Kaiser, A. Varzi and S. Passerini, *Adv. Energy Mater.*, 2019, **9**, 1902077.
151 Y. Ma, U. Ulissi, D. Bresser, Y. Ma, Y. Ji and S. Passerini, *Electrochim. Acta*, 2017, **258**, 535–543.
152 Y. Oumellal, A. Rougier, G. A. Nazri, J. M. Tarascon and L. Aymard, *Nat. Mater.*, 2008, **7**, 916–921.
153 D. Weber, Đ. Tripković, K. Kretschmer, M. Bianchini and T. Brezesinski, *Eur. J. Inorg. Chem.*, 2020, 3117–3130.
154 Y. Qi, N. Du, H. Zhang, P. Wu and D. Yang, *J. Power Sources*, 2011, **196**, 10234–10239.
155 K. Xu, *Chem. Rev.*, 2014, **114**, 11503–11618.
156 F. Fan, G. Fang, R. Zhang, Y. Xu, J. Zheng and D. Li, *Appl. Surf. Sci.*, 2014, **311**, 484–489.
157 Y. Ma, Y. Ma, G. Giuli, H. Euchner, A. Groß, G. O. Lepore, F. D'Acapito, D. Geiger, J. Biskupek, U. Kaiser, H. M. Schütz, A. Carlsson, T. Diemant, R. J. Behm, M. Kuenzel, S. Passerini and D. Bresser, *Adv. Energy Mater.*, 2020, **10**, 2000783.
158 W. Cheng, F. Rechberger, G. Ilari, H. Ma, W. I. Lin and M. Niederberger, *Chem. Sci.*, 2015, **6**, 6908–6915.
159 Y. Ma, Y. Ma, U. Ulissi, Y. Ji, C. Streb, D. Bresser and S. Passerini, *Electrochim. Acta*, 2018, **277**, 100–109.
160 K. Liang, T. Y. Cheang, T. Wen, X. Xie, X. Zhou, Z. W. Zhao, C. C. Shen, N. Jiang and A. W. Xu, *J. Phys. Chem. C*, 2016, **120**, 3669–3676.
161 Y. Ma, Y. Ma, D. Geiger, U. Kaiser, H. Zhang, G.-T. Kim, T. Diemant, R. J. Behm, A. Varzi and S. Passerini, *Nano Energy*, 2017, **42**, 341–352.
162 Z. Wang, Z. Wang, W. Liu, W. Xiao and X. W. Lou, *Energy Environ. Sci.*, 2013, **6**, 87–91.
163 A. Varzi, L. Mattarozzi, S. Cattarin, P. Guerriero and S. Passerini, *Adv. Energy Mater.*, 2018, **8**, 1701706.
164 A. González, E. Goikolea, J. A. Barrena and R. Mysyk, *Renewable Sustainable Energy Rev.*, 2016, **58**, 1189–1206.
165 X. Lu, T. Liu, T. Zhai, G. Wang, M. Yu, S. Xie, Y. Ling, C. Liang, Y. Tong and Y. Li, *Adv. Energy Mater.*, 2014, **4**, 1300994.
166 J. Li, Q. Fang and P. K. Liaw, *Adv. Eng. Mater.*, 2021, **23**, 2001044.
167 M. Widom, *J. Mater. Res.*, 2018, **33**, 2881–2898.
168 Z. Zhou, Y. Zhou, Q. He, Z. Ding, F. Li and Y. Yang, *npj Comput. Mater.*, 2019, **5**, 128.
169 P. C. Vilalta, S. Sheikholeslami, K. Saleme Ruiz, X. C. Yee and M. Koslowski, *J. Eng. Mater. Technol.*, 2021, **143**, 1–8.
170 J. M. Rickman, G. Balasubramanian, C. J. Marvel, H. M. Chan and M.-T. Burton, *J. Appl. Phys.*, 2020, **128**, 221101.
171 Y. Zhang, C. Wen, C. Wang, S. Antonov, D. Xue, Y. Bai and Y. Su, *Acta Mater.*, 2020, **185**, 528–539.
172 D. Dai, T. Xu, X. Wei, G. Ding, Y. Xu, J. Zhang and H. Zhang, *Comput. Mater. Sci.*, 2020, **175**, 109618.
173 Z. Pei, J. Yin, J. A. Hawk, D. E. Alman and M. C. Gao, *npj Comput. Mater.*, 2020, **6**, 50.
174 C. Wen, Y. Zhang, C. Wang, D. Xue, Y. Bai, S. Antonov, L. Dai, T. Lookman and Y. Su, *Acta Mater.*, 2019, **170**, 109–117.
175 K. Kaufmann and K. S. Vecchio, *Acta Mater.*, 2020, **198**, 178–222.
176 W. Huang, P. Martin and H. L. Zhuang, *Acta Mater.*, 2019, **169**, 225–236.
177 Y. J. Chang, C. Y. Jui, W. J. Lee and A. C. Yeh, *JOM*, 2019, **71**, 3433–3442.
178 R. Machaka, *Comput. Mater. Sci.*, 2021, **188**, 110244.
179 K. Kaufmann, D. Maryanovsky, W. M. Mellor, C. Zhu, A. S. Rosengarten, T. J. Harrington, C. Oses, C. Toher, S. Curtarolo and K. S. Vecchio, *npj Comput. Mater.*, 2020, **6**, 42.
180 G. Kim, H. Diao, C. Lee, A. T. Samaei, T. Phan, M. de Jong, K. An, D. Ma, P. K. Liaw and W. Chen, *Acta Mater.*, 2019, **181**, 124–138.
181 T. Kostiuchenko, F. Körmann, J. Neugebauer and A. Shapeev, *npj Comput. Mater.*, 2019, **5**, 55.
182 G. M. Tomboc, T. Kwon, J. Joo and K. Lee, *J. Mater. Chem. A*, 2020, **8**, 14844–14862.
183 Z. Lu, Z. W. Chen and C. V. Singh, *Matter*, 2020, **3**, 1318–1333.
184 H. Ji, A. Urban, D. A. Kitchaev, D.-H. Kwon, N. Artrith, C. Ophus, W. Huang, Z. Cai, T. Shi, J. C. Kim, H. Kim and G. Ceder, *Nat. Commun.*, 2019, **10**, 592.
185 W. Xu, H. Chen, K. Jie, Z. Yang, T. Li and S. Dai, *Angew. Chem., Int. Ed.*, 2019, **131**, 5072–5076.
186 C. Yuan, H. Bin Wu, Y. Xie and X. W. Lou, *Angew. Chem., Int. Ed.*, 2014, **53**, 1488–1504.